DTIC FILE COPY

(1)

AD-A227 734

1990 Thesis/Dissertation

Low Frequency Predictability of Dynamical Extended Range Forecast Experiments

Dennis Alan Rodgers

AFIT Student at: University of Utal

AFIT/CI/CIA - 90-082

AFIT/CI
Wright-Patterson AFB OH 45433

Approved for Public Release IAW AFR 190-1
Distribution Unlimited
ERNEST A. HAYGOOD, 1st Lt, USAF
Executive Officer, Civilian Institution Programs

DTIC
ELECTE
OCT 23 1990
S B D

82

UNCLASSIFIED

90 10 22 088

Low Frequency Predictability of Dynamical Extended Range Forecast Experiments

Dennis Alan Rodgers

Capt USAF

Year: 1990

82 pages

Master of Science

University of Utah

ABSTRACT

The tropical intraseasonal oscillation is examined using projections of 5-day averaged wind and height data onto the normal modes of a primitive equation model lineraized about a basic state at rest and prescribed global temperature. The data set utilized in this study is from the Dynamical Extended Range Forecast (DERF) Experiment, conducted from January 1986 to March 1987.

The examination of zonal wind anomalies in the tropics shows that the forecast model is unable to accurately predict either the amplitude or propagation of the 30-50 day oscillation, even when it is well-defined in the analysis. The forecasted amplitude is always much weaker than what the analysis data indicate.

While errors are found in the tropical divergent wind field, the current study does not permit conclusions to be drawn regarding the influences of these errors, if any, on the extratropics. On the other hand, error patterns in the rotational wind fields of the extratropics, especially the Northern Hemisphere, are found to propagate into tropical regions. This is best seen in the internal Rossby modes. Extratropical error patterns in the external Rossby modes, which are significantly larger in magnitude, are found to be mostly stationary. However, since these errors extend into tropical regions, the rotational error fields in the tropics closely resemble their extratropical counterparts.

Internal Rossby modes are found to constitute only around 35 percent of the total rotational flow in the extratropics of the Northern Hemisphere at 700 mb. However, their contribution to the error field is rather large when compared to those of the external Rossby modes. Improvement of extratropical forecasts depends on

better specification of stationary barotropic rotational motions and suppression of spurious propagating internal Rossby modes.

Most of the rotational error in the tropics is imported from the extratropics, and therefore, improvement in rotational tropical motions depends on better simulation of extratropical circulations. On the other hand, divergent wind errors do not appear to be linked to those in the extratropics. Therefore, improvements in tropical forecasts of the divergent wind rely on more accurate specification of tropical forcing and dynamics.

Accession For	
NTIS GRA&I	☒
DTIC TAB	☐
Unannounced	☐
Justification	
By	
Distribution/	
Availability Codes	
Dist	Avail and/or Special
A-1	

REFERENCES

Chen, T. -C., and J. C. Alpert, 1989: The systematic errors of annual and intraseasonal variations of the planetary-scale divergent circulation in NMC medium range forecasts (in preparation).

Chen, W. Y., 1989: Estimate of dynamical predictability from NMC DERF experiments. *Mon. Wea. Rev.*, **117**, 1227-1236.

Emanuel, K. A., 1987: An air-sea interaction model of intraseasonal oscillations in the tropics. *J. Atmos. Sci.*, **44**, 2334-2340.

Ferranti, L., T. N. Palmer, F. Molteni and E. Klinker, 1990: Tropical-extratropical interaction associated with the 30-60 day oscillation, and its impact on medium and extended range predictability. Submitted to *J. Atmos. Sci.*

Hayashi, Y. -Y., and A. Sumi, 1986: The 30-40 day oscillations simulated in an aqua planet model. *J. Meteor. Soc. Jpn.*, **64**, 451-466.

Kalnay, E., R. Gardner, H. -L. Pan, M. Kanamitsu and G. White, 1988: Precipitation and surface properties in the NMC global model: systematic characteristics and predictability. *WGNE Workshop on Model Systematic Errors*, Toronto, Canada, September 19-23, 1988.

Kasahara, A., 1979: Normal modes of ultralong waves in the Atmosphere. *Mon. Wea. Rev.*, **104**, 669-690.

___, and K. Puri, 1981: Spectral representation of three-dimentional global data by expansion in normal mode funcitons. *Mon. Wea. Rev.*, **109**, 37-51.

Lau, K. -M., and P. H. Chan, 1985: Aspects of the 40-50 day oscillation during the northern winter as inferred from outgoing longwave radiation. *Mon. Wea. Rev.*, **113**, 1889-1909.

Lee, B. -C., 1987: Observed normal mode structure of low frequency oscillations. Doctoral dissertation, University of Utah, 160 pp.

Lorenz, E. N., 1968: The predictability of a flow which possesses many scales of motion. *Tellus*, **21**, 289-307.

Madden, R. A., and P. A. Julian, 1971: Detection of a 40-50 day oscillation in the zonal wind in the tropical pacific. *J. Atmos. Sci.*, **28**, 702-708.

___, and___, 1972: Description of global-scale circulation cells in the tropics with a 40-50 day period. *J. Atmos. Sci.*, **29**, 1109-1121.

LOW FREQUENCY PREDICTABILITY OF DYNAMICAL EXTENDED RANGE FORECAST EXPERIMENTS

by

Dennis Alan Rodgers

A thesis submitted to the faculty of
The University of Utah
in partial fulfillment of the requirements for the degree of

Master of Science

Department of Meteorology

University of Utah

June 1990

Copyright © 1990 Dennis Alan Rodgers

All Rights Reserved

THE UNIVERSITY OF UTAH GRADUATE SCHOOL

SUPERVISORY COMMITTEE APPROVAL

of a thesis submitted by

Dennis Alan Rodgers

This thesis has been read by each member of the following supervisory committee and by majority vote has been found to be satisfactory.

May 16, 1990 — Chair: Julia N. Paegle

May 16, 1990 — Kou-Nan Liou

May 16, 1990 — Kingtse Mo

THE UNIVERSITY OF UTAH GRADUATE SCHOOL

FINAL READING APPROVAL

To the Graduate Council of the University of Utah:

I have read the thesis of Dennis Alan Rodgers in its final form and have found that (1) its format, citations, and bibliographic style are consistent and acceptable; (2) its illustrative materials including figures, tables, and charts are in place; (3) the final manuscript is satisfactory to the Supervisory Committee and is ready for submission to the Graduate School.

May 16, 1990
Date

Julia N. Paegle
Chair, Supervisory Committee

Approved for the Major Department

J.E. Geisler
Chair/Dean

Approved for the Graduate Council

B. Gale Dick
Dean of The Graduate School

ABSTRACT

The tropical intraseasonal oscillation is examined using projections of 5-day averaged wind and height data onto the normal modes of a primitive equation model lineraized about a basic state at rest and prescribed global temperature. The data set utilized in this study is from the Dynamical Extended Range Forecast (DERF) Experiment, conducted from January 1986 to March 1987.

The examination of zonal wind anomalies in the tropics shows that the forecast model is unable to accurately predict either the amplitude or propagation of the 30-50 day oscillation, even when it is well-defined in the analysis. The forecasted amplitude is always much weaker than what the analysis data indicate.

While errors are found in the tropical divergent wind field, the current study does not permit conclusions to be drawn regarding the influences of these errors, if any, on the extratropics. On the other hand, error patterns in the rotational wind fields of the extratropics, especially the Northern Hemisphere, are found to propagate into tropical regions. This is best seen in the internal Rossby modes. Extratropical error patterns in the external Rossby modes, which are significantly larger in magnitude, are found to be mostly stationary. However, since these errors extend into tropical regions, the rotational error fields in the tropics closely resemble their extratropical counterparts.

Internal Rossby modes are found to constitute only around 35 percent of the total rotational flow in the extratropics of the Northern Hemisphere at 700 mb. However, their contribution to the error field is rather large when compared to those of the external Rossby modes. Improvement of extratropical forecasts depends on

better specification of stationary barotropic rotational motions and suppression of spurious propagating internal Rossby modes.

Most of the rotational error in the tropics is imported from the extratropics, and therefore, improvement in rotational tropical motions depends on better simulation of extratropical circulations. On the other hand, divergent wind errors do not appear to be linked to those in the extratropics. Therefore, improvements in tropical forecasts of the divergent wind rely on more accurate specification of tropical forcing and dynamics.

TABLE OF CONTENTS

ACKNOWLEDGMENTS

I would like to express my sincere appreciation to my advisor, Dr. Julia N. Paegle, for her guidance and encouragement throughout this work. Her knowledge and special insights into the subject matter were critical for this project's eventual completion. I also want to thank the other members of my supervisory committee, Dr. Kuo-Nan Liou and Dr. Kingste Mo, for their advice and helpful suggestions. Dr. Mo was also kind enough to supply me with rainfall and surface heat flux data neccessary for this study.

I am also indebted to Estella Collini for sharing her vast computer knowledge with me during the early stages of this research. I would also like to thank John Close for his friendship, encouragement, and inspiration over the past two years. Finally, a special thanks to my wife Michelle, whose patience and support contributed subtantially to the successful completion of this paper. I could not have done this without her.

CHAPTER 1

INTRODUCTION

The main goal of this investigation is to analyze data from the Dynamical Extended Ranage Forecast (DERF) Experiment and determine the differences between the analysis and forecasts with emphasis on the tropical 30-50 day oscillation. These differences will help access whether the forecast model is able to maintain the signature of the oscillation observed in nature. The diagnostic tool used is the projection of the analysis and forecast data onto the normal modes of a primitive equation model. This modal breakdown may be useful to suggest methods to improve long-range forecasts and enhance predictabilitiy.

A low frequency oscillation with a period range of 30-50 days was first documented by Madden and Julian (1971,1972). Using spectral and cross-spectral analysis on rawinsonde data for Canton Island (3° S, 172° W) and other tropical stations, they determined that this oscillation extends around the globe and is confined to the tropics. It possesses features of a baroclinic, eastward moving wave whose characteristics change with time (Madden and Julian, 1972). Figure 1.1 summarizes their hypotheses regarding the time and space variations of the disturbance associated with the 30-50 day oscillation. This disturbance is strongest around Indonesia and the extreme western Pacific with well-defined circulation patterns and widespread convection. As it moves eastward, the disturbance weakens dramatically over the central and eastern Pacific. It then begins to strengthen over the Indian Ocean. Madden and Julian concluded that a tropical oscillation of this

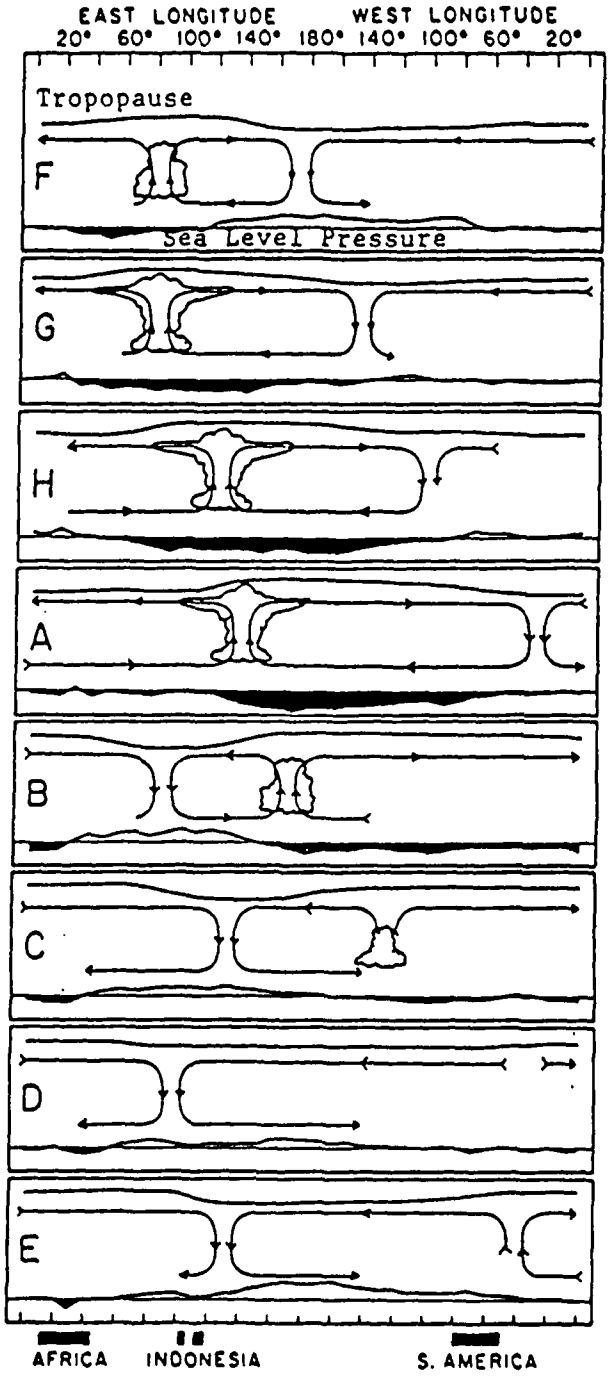

Figure 1.1. Schematic depiction of the time and space (zonal plane) variation of circulation cells associated with the 30-50 day oscillation. The mean pressure disturbance is ploted at the bottom of each chart with negative anomalies shaded. Areas of enhanced, widespread convection are indicated by the cumulus and cumulonimbus clouds. The relative tropopause height is shown at the top of each chart (from Madden and Julian (1972), reprinted with permission of the American Meteorological Society).

size must affect circulation patterns in other latitudes.

Lau and Chan (1985) identified extratropical outgoing longwave radiation (OLR) anomalies, which evolve inherently with the 30-50 day oscillation. They showed that when the convective centers are located over the Indian Ocean and equatorial western Pacific, major extratropical anomalies are found over the Asian sector. When the convective centers shift eastward over the maritime continent and the equatorial central Pacific (approximately 3000-4000 km), the extratropical anomalies are largest over the eastern North Pacific. This suggests possible connections between tropical and extratropical circulation/convection patterns, and underscores the importance of understanding this oscillation.

Many theoretical explanations have been proposed in recent years to explain this phenomenon. These explanations can be grouped into the following categories: localized heat source over the equatorial Asian monsoon region, traveling heat source with a CISK (conditional instability of the second kind) mechanism responsible for sustaining the disturbance, and boundary forcing.

Of particular interest is the boundary forcing solution advanced by Emanuel (1987) and Neelin et al. (1987). They proposed an air-sea interaction model where convection is not a heat source in and of itself, but acts to redistribute aloft heat acquired from the sea surface. In this model, latent and sensible heat fluxes from the sea surface are the driving mechanisms of the oscillation, with perturbation surface easterlies coinciding with surface fluxes and warming (Nogues-Paegle et al., 1989). This explanation matches well with the results of Madden and Julian (see Fig. 1.1), in which the disturbance weakens dramatically over the cold ocean waters of the eastern Pacific.

Nogues-Paegle et al. (1989) examined the three-dimensional structure of the tropical 30-50 day oscillation by projecting weekly averaged height and wind data

onto the normal modes of a primative equation model. They found an eastward propagation in the Kelvin (K), first Rossby (R1), and second Rossby (R2) modes. The total energy for these modes is greatest for zonal wavenumber 1 and a vertical structure that reverses in height at around 500 mb (256 m equivalent depth). Past theoretical studies have linked the K and R1 modes to tropical convection and air-sea interaction. Additionally, the amplitude of the R1 mode is smaller than that of the K mode. Interestingly enough, the K and R1 modes both amplify over the cold waters of the central and eastern Pacific Ocean during the second propagation cycle. This contradicts past studies that predict a decay in the oscillation over areas where heating is cut off.

An observational and modeling study examining tropical/extratropical interactions associated with the 30-50 day oscillation was performed by Ferranti et al. (1990). After identifying periods when the ocillation was active by an empirical orthogonal function analysis (EOF) of OLR data, they used relaxation of the model fields to investigate the impact of the tropics on the extratropics in an NWP model. They found that for medium and long range predictions, this impact is typically quite large. They conclude that skillful prediction of the large-scale tropical flow is a prerequisite for extratropical extended-range prediction.

Tropical diabatic heating is largely responsible for the planetary-scale divergent circulation. Because divergent circulation is well-depicted by velocity potential, Chen and Alpert (1989) performed a EOF analysis on the 30-60 day filtered 200 mb velocity potential fields of forecasts made by the National Meteorological Center's (NMC) Medium Range Forecast (MRF) model. By examining the first two eigenmodes (which make up the eastward propagating, low frequency mode), they discovered that the oscillation loses amplitude and is not recognizable after day 5 of the forecasts. However, if the low frequency mode is quite large, as it was during

the 1987-1988 winter season, the model can maintain the signature of the oscillation for a longer time period. While the eastward propagation of this low frequency mode is generally well-predicted, the model does tend to systematically increase the propagation rate as the forecast time becomes longer.

Tsuyuki (1989) investigated the relationship between the tropical 30-50 day oscillation and the predictability of extratropical circulations using operational 15-day forecasts produced by the global prediction model of the Japan Meteorological Agency (JMA). He found that the model is quite successful in predicting both the amplitude and phase of the eastward propagating 30-50 day modes when they are significant in the observation. He attributes this success to massive revisions in the model (1988), which substantially improved the forecast of the planetary-scale tropical divergence fields. Also, when the eastward propagating 30-50 day modes are well-predicted, the extended-range forecasts for the Northern Hemisphere improve, and have a relatively high skill level. Tsuyuki concludes that improvement in the prediction of the tropical 30-50 day oscillation is vital to the eventual success of long-range extratropical forecasts.

How well the NWP models forecast the 30-50 day oscillation obviously impacts long-range forecasts around the globe. In this study, tropical and extratropical forecasts are examined when the 30-50 day oscillation is well-defined and when it is quite weak. Does its presence degrade model performance, or does the periodicity of the oscillation improve the output?

The primary data set used in this study is from the Dynamical Extended Range Forecast (DERF) Experiment. A general discription of the DERF data is provided in Chapter 2.

CHAPTER 2

DATA PROCESSING

2.1 General Description of the DERF Data

The primary objective of NMC's Dynamical Extended Range Forecasting (DERF) experiment was to assess the feasibility of extending operational numerical weather prediction beyond the medium range (Traction et al., 1989). The basic elements of the program were threefold: model development, creation of a very rich data base of experimental extended range predictions, and evaluation of the results (Tracton et al., 1989). The model used was the latest available version of the MRF, MRF86 (Tracton et al., 1989). Since the time of the experiment, several changes have been made to improve the model output. One of the most important physical processes recently added to the model is the interaction of clouds and radiation. During the DERF experiments, climatological values of zonally averaged clouds were used, which contributed to poor definition of convection in the tropics. Other improvements include the parameterization of gravity wave drag caused by topography and the formulation of surface evaporation (Kalnay et al., 1988).

The global data base utilized in this investigation is from Phase II of the experiment. It consists of 108 contiguous 30-day forecasts from initial conditions 24 hours apart between 14 December 1986 and 31 March 1987 (Tracton et al., 1989). A reduced version of these data is available for research. Schubert et al. (1988) describes in detail the sample fields and data reduction. Surface fields have resolution of 4 degrees in latitude by 5 degrees in longitude. These fields consist of surface

temperature, soil moisture, snow depth, total rainfall, convective rainfall, surface sensible heat flux, surface latent heat flux, surface u-stress, and surface v-stress. The remaining data are in spherical harmonic coefficient form, with T20 truncation. This includes ln(surface pressure) and certain upper-air parameters. Most upper level quantities are at the 11 mandatory levels: 1000 mb, 850 mb, 700 mb, 500 mb, 400 mb, 300 mb, 250 mb, 200 mb, 150 mb, 100 mb, and 50 mb. These fields consists of geopotential height, ucos(latitude), vcos(latitiude), and temperature. Vertical velocity and relative humidity extend up to 100 mb and 300 mb, respectively.

2.2 Results of Past Studies Using DERF II Data

Many studies have already examined some aspects of model performance during the DERF II period. Tracton et al. (1989) investigated the 108 case average forecast and found that while stationary waves and the zonal mean wind were predicted well, a systematic tendency to over forecast the mid-latitude zonal flow was present. This error, however, has since been reduced by the introduction of the gravity wave drag parameterization to the model in 1987 (Kalnay et al., 1988). Additionally, an examination of the 1000-500 mb thickness showed a cold bias in the stratosphere over nearly the entire globe. This bias is especially strong over North America, and shows a continuous increase through out the 30-day forecast period. They also found that in the 1-30 day means, the model is generally more skillful than persistence. Interestingly enough, the best possible estimate of the 30-day mean circulation is found in the average of the first 7-10 days of the forecast, not in the 30-day mean.

Kalnay et al. (1988) investigated the DERF period average of the day 1 and day 30 forecasts of precipitation, to identify any systematic characteristics of the model.

They found the day 1 forecast to be excellent when compared to climatology. Even after 30 days, the precipitation field was realisitic, despite a strong underestimation of precipitation over southern Africa and the Amazons, compensated by a shift in the rain towards the east coast of Africa, South America, and Australia. The predictability of instantaneous precipitation, however, deteriorates very quickly with time. While extratropical rain in the Northern Hemisphere was found to be more predictable than elsewhere, even there an anomaly correlation of 0.6 is attained in under 2 days. This fast decay comes about because instantaneous precipitation is associated with small horizontal scales, which obviously have short dynamical predictability.

Using the DERF II data, Chen (1989) obtained estimates of dynamical predictability for the forecast model. He concluded that the skill level obtained is well below its potential, meaning there is ample room for improvement. He also estimates that if the model was eventually made perfect, 10-day forecasts could become as skillful as the current 6-day forecasts. Additionally, if initial data errors were reduced substantially, this forecast period could be extended to approximately 14 days.

2.3 Manipulation of DERF II Data for This Study

Despite remarkable advances in the field of numerical weather prediction over the past 70 years, the fact remains that atmospheric processes have a finite range of predictability. According to studies on the subject, the limit of predictability for individual weather systems is about 2 weeks (Lorenz, 1968). Roads (1986) found that useful forecast intervals for time averages can be substantially longer than those for instantaneous events. This extension in predictability arises from the averaging process, which suppresses less predictable, high frequency components

of the circulation (Tracton et al., 1989). Additionally, time averaging is one way to isolate low frequency variablility (Tsuyuki, 1989). Because this study centers around the 30-50 day oscillation, a time averaging approach is utilized.

Numerous manipulations had to be performed on the DERF II data set before it was useful for this study. The manipulations for both the surface gridded data and the spherical harmonic coefficient data will be outlined now.

The surface fields of interest in this study, with a grid resolution of 4 degrees in latitude by 5 degrees in longitude, are total rainfall, convective rainfall, sensible heat flux, and latent heat flux. The first 24 hour forecasts of these fields are considered to represent the observed conditions, and will be referred to as the analysis from now on. First, a 5-day (pentad) averaging process was performed on the analysis data, beginning with the 17 December 1986 analysis. Thus, 21 cases of pentad-averaged data were constructed for each of these four data fields. The first 3 days of the DERF period, 14-16 December 1986, were also averaged and included as a pentad average, bringing the number of analysis cases to 22.

Next, pentad averages were performed on selected forecasts for these four data fields. To match the analysis cases for later comparisons, forecasts beginning 17 December and every 5 days thereafter were used. Each forecast set contains 30 individual forecasts; thus, six pentad averages were produced for each forecast set. So there are 21 forecast cases, each with six pentad averages.

Manipulation of the data sets in spherical harmonic coefficent format (also called complex spectral coefficent format) was much more complex. The data of interest here are the surface pressure (p), geopotential height (z), the zonal (u) and meridional (v) components of the wind, temperature (t), and vertical velocity (w). With the exception of the p and w fields, there are data for all 11 mandatory levels in the atmosphere. The vertical velocity fields only extend through the first 10 levels.

The pentad-averaging procedure used for the analysis and forecast data described above was also utilized for these data sets. Because the analysis data for these fields extend to 6 April (beyond 31 March), we have 24 analysis cases as compared to just 22 above. Additionally, forecast data from 31 January 1987 were missing for these data fields; thus, there are 20 forecast cases, each with six pentad averages.

After completing the averaging process, the next step was to convert the data from spectral coefficient format to a grid format. The grid chosen consists of 72 latitude points and 37 longitude points. The (72,37) grid was obtained specifying to a T21 truncation, and not a T20 truncation as stated in earlier DERF literature.

Next, the u,v, and z data were interpolated to designated sigma levels (σ = .95, .9, .8, .7, .6, .5, .4, .3, .2, .1, .05). To do this interpolation, surface pressure in a consistent form was obtained by using height data at all 11 vertical pressure levels and the surface topography.

2.4 Normal Mode Projection

The projection of data onto the normal modes of a primitive equation model offers several distinct advantages over single variable analyses. First, it allows for the differentiation of contributions from different vertical modes (Kasahara, 1976). Additionally, the horizontal structures permit the simultaneous analysis of both the wind and the mass fields (Nogues-Paegle et al., 1989). This makes it possible to examine two distinct types of motion: high frequency waves (inertia-gravity modes) and low frequency waves (rotational modes of the Rossby/Haurwitz type). Using normal mode projection as a diagnostic tool allows focusing on atmospheric structures that are not altered by the assimilating model. (Nogues-Paegle et al., 1989).

Normal mode projection is outlined in detail by Kasahara and Puri (1981).

Nogues-Paegle et al. (1989) used this procedure to examine data collected during the 1979 Global Weather Experiment. In this investigation, the three-dimensional z, u, and v fields are projected onto the normal modes of a primitive equation model linerized about a basic state at rest and the vertically-varied global average temperature for the DERF period:

$$z,u,v(\lambda,\phi,\sigma) = \sum_{m=1}^{10}\sum_{n=1}^{10}\sum_{s=1}^{11} X_n^m(s)H_n^m(\phi,s)\Gamma(s)e^{ik_m x}$$

where:

X = wave coefficient

H = Hough function (horizontal structure function)

Γ = vertical structure function

λ = longitude

ϕ = latitude

m = zonal wave number

n = meridional index

s = vertical index

As was stated earlier, this projection allows the data to be broken down into different horizontal and vertical modes. There are 10 zonal, 10 meridional, and 11 vertical components. Figure 2.1 shows the first five vertical structure functions for the DERF data, along with the corresponding equivalent depths. The first vertical mode (equivalent depth of 9459 m) increases slightly with height and has no zero crossing points. The horizontal divergence profile of this mode is the same sign throughout the depth of the atmosphere. It is called the external or barotropic mode. The others have height reversals and are labeled internal or baroclinic modes (the second vertical mode is essentially barotropic in the troposphere and baroclinic

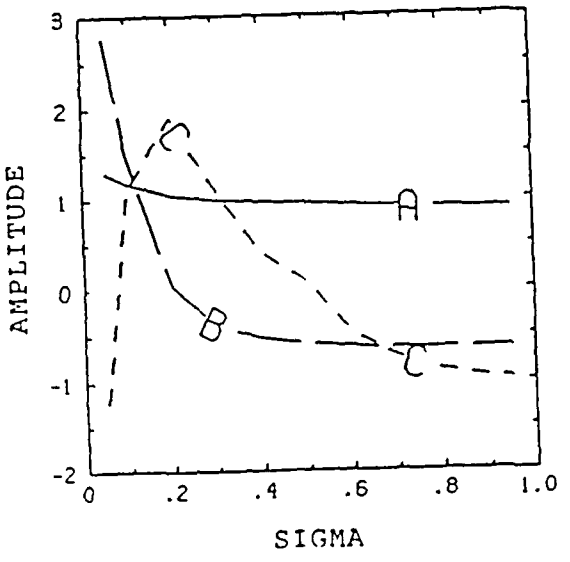

A 9459 m
B 1461 m
C 235 m
D 93 m
E 41 m

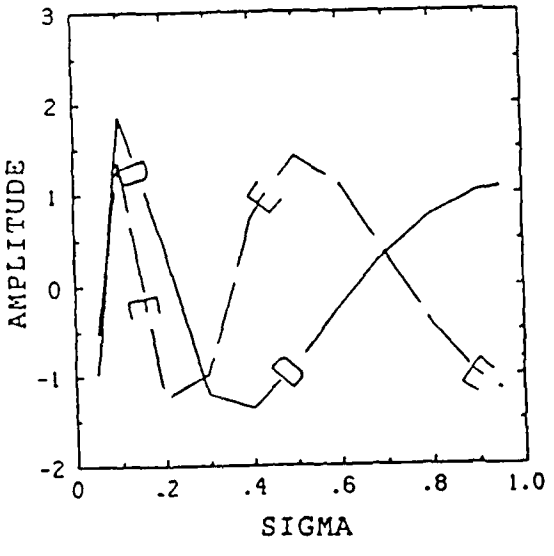

Figure 2.1. Vertical structure functions for DERF data. The equivalent depth for each vertical mode is given at right. The modes are ordered in terms of decreasing equivalent depth.

in the statosphere). This study is concerned with deep atmospheric motion, which is mostly contained in the first five vertical modes.

The meridional modes can be decomposed into Rossby (R), eastward gravity (EG), and westward gravity (WG) wave components. The phase speed of the Rossby modes is slower than that of the gravity modes, so they can generally be distinguished from each other fairly easily. This modal breakdown is helpful in describing the nature of tropical/extratropical interactions, since Hadley cells project mostly into the internal gravity modes while mid-latitude flows project mainly into the external Rossby modes (Matsuno, 1966).

Because the 30-50 day oscillation has maximum zonal wind at the equator, those meridional modes with this type of structure are of particular interest in this study. Kelvin modes, which have characteristics of both Rossby and gravity modes but behave as pure gravity modes in the x-direction, are clear examples (Fig. 2.2). Additionally, because the time period of the DERF experiment was during Northern Hemisphere winter, the maximum heating was just off the equator in the Southern Hemisphere. Thus, meridional modes that have a maximum zonal wind within 25 degrees of the equator are also of great interest. Examples of these modes include the external and first internal Rossby modes, where the zonal wind maximizes at about 13 degrees and 25 degrees, respectively (see Fig. 2.3).

After projecting our data onto the normal modes, the next step is to reconstruct the u,v, and z fields by resumming the wave coeffiecients (X) over all the R, EG, and WG modes, as well as over the external (s = 1) and deep internal (s = 2-5) vertical modes. This is done for only one level in the atmosphere, σ = .7. The Kelvin modes are included as part of the EG modes.

To be certain the normal mode projection and resumming procedures were done correctly, the analysis wind data for January 1987 were averaged and then projected

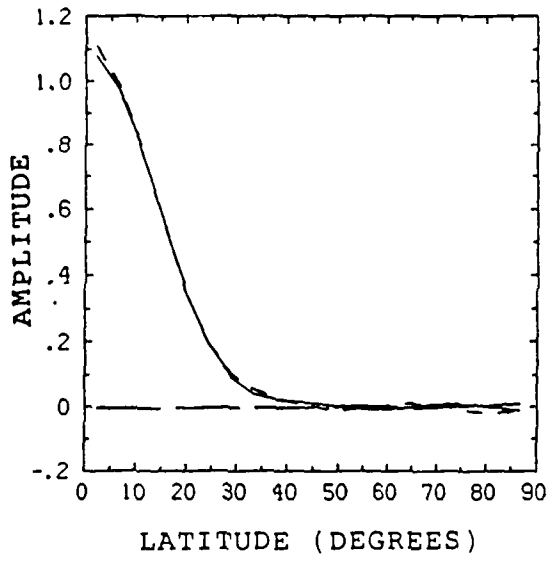

Figure 2.2. Horizontal structure functions for the Kelvin mode, with zonal wave number 1 and vertical mode 3. The solid line indicates the zonal wind component, the long dashed line depicts the meridional wind component, and the short dashed line is for the height.

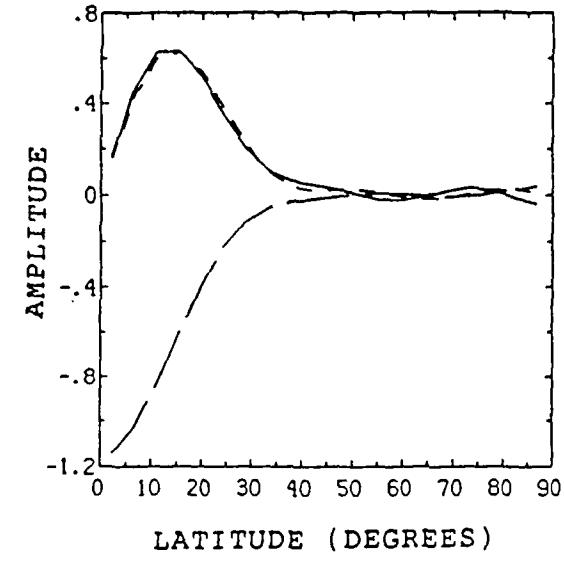

a

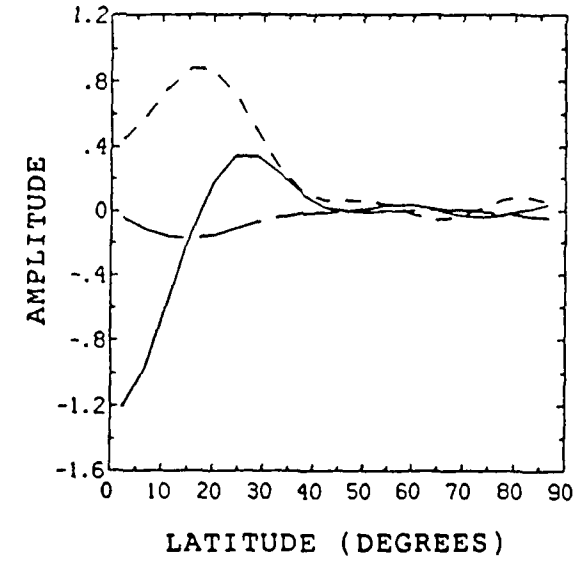

b

Figure 2.3. Horizontal structure functions for (a) the first asymetric, second internal Rossby mode and (b) the first symetric, second internal Rossby mode. The solid line indicates the zonal wind component, the long dashed line depicts the meridional wind component, and the short dashed line is for the height.

and resummed as outlined earlier. However, in this case the resumming was for $\sigma =$ .2, since January wind averages were readily available from the Climatic Diagnostic Bulletin of the Climate Analysis Center (CAC)/NMC/NOAA for comparison. Next, the R, EG, and WG components were added together to give the total wind contained in vertical modes 1-5 as well as 1-11 (the complete wind field). This was then compared to the average January 1987 $\sigma = .2$ wind field using analysis data before the projection and available CAC maps. The results were very similar, proving that the projection and resumming were correct and that the data were correctly read. Additionally, this comparison confirmed that the deep vertical modes (1-5) contain nearly all of the total energy.

CHAPTER 3

INTRASEASONAL OSCILLATION DURING DERF PERIOD

3.1 Introduction

In this chapter, the DERF period analysis data will be examined, with special emphasis on obtaining the signature of the tropical 30-50 day oscillation. The modal breakdown discussed in Chapter 2 will be utilized in this analysis. This will illustrate the convenience and usefulness of examining the various horizontal modes instead of just the total z,u and v fields. For this study, the tropics are defined as 20° N - 20° S, the Northern Hemisphere as 20° N - 80° N, and the Southern Hemisphere as 20° S - 80° S. As outlined in Chapter 2, the internal modes consist of contributions from vertical modes 2 through 5 only, while the external modes (or barotropic modes) consist of vertical mode 1.

3.2 Examination of DERF Analysis Data

As discussed in Chapter 2, the projection of height and wind data onto normal mode functions allows the analysis of both wind and mass fields simultaneously. Thus, it is possible to separate the energy into two distinct kinds of motions, inertia-gravity modes and Rossby/Haurwitz type rotational modes. In this section, the DERF period average wind and geopotential fields will be examined to compare the mass/wind balance of the Rossby and gravity components. The geopotential

field is used in the normal mode projections in σ coordinates, and is defined as:

$$H = gz + RT(ln(Ps))$$

where g is gravity, z is height, R is the gas constant for dry air, T is the temperature, and Ps is a nondimensional surface pressure.

Rossby modes should exhibit a nearly geostrophic balance between the mass and wind fields. Figure 3.1 shows the DERF period average wind and geopotential field for the external Rossby component at $\sigma = .7$. The wind and mass fields are generally in geostrophic balance, which is demonstated by the parallel configuration of the wind vectors and the geopotential contours. This is especially true in the Southern Hemisphere where the flow is mainly zonal. In the Northern Hemsiphere, a slight imbalance can be noted, especially where troughs and ridges are present. A similiar field for $\sigma = .3$ is almost identical to Fig. 3.1, except for a slight increase in the magnitude of the wind (not shown). This is to be expected because of the barotropic structure through the atmosphere of the first vertical mode (see Fig. 2.1).

The internal Rossby components at $\sigma = .7$ and $\sigma = .3$ are shown in Fig. 3.2. Here, again, there is a general balance between the mass and wind fields, although a slight imbalance does exist in areas of troughs and ridges. Important differences, however, do exist between the two levels. At $\sigma = .7$ (Fig. 3.2a), an easterly flow is present at all latitudes. Higher in the atmosphere at $\sigma = .3$ (Fig. 3.2b), there is a strong westerly flow in mid-latitudes, especially in the Northern Hemisphere over the western and central Pacific. Thus, the internal Rossby modes display strong vertical wind shear. This basic pattern of wind speed increasing with height and a reversal in wind direction suggests that vertical mode 3 contains most of the total energy.

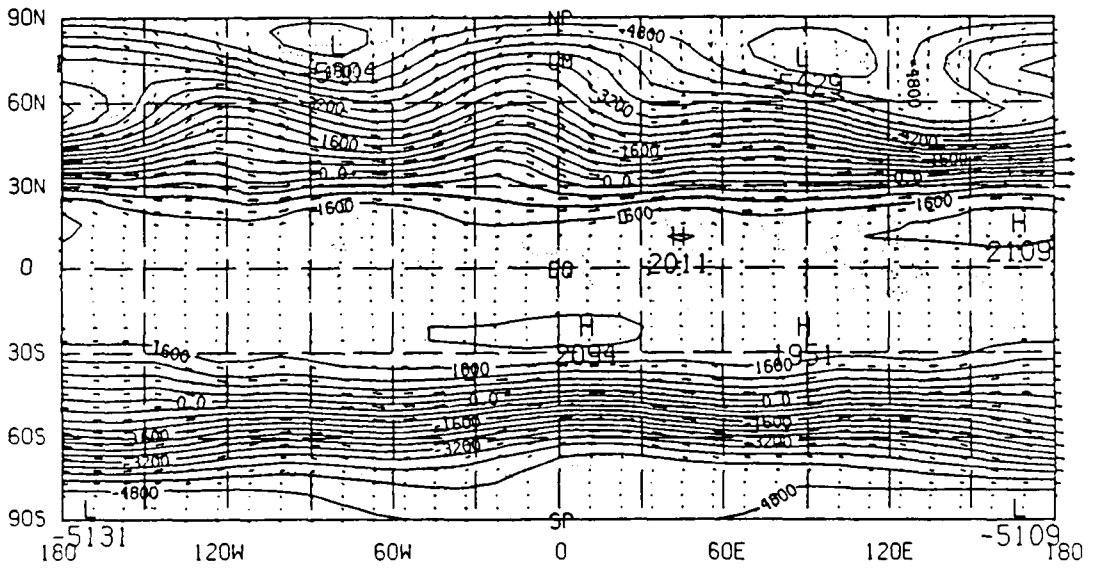

Figure 3.1. DERF period average wind vectors (m/s) with geopotential deviations from a global constant, contoured every 400 m^2/s^2 for the external Rossby component at $\sigma = .7$. The maximum vector is 31.8 m/s.

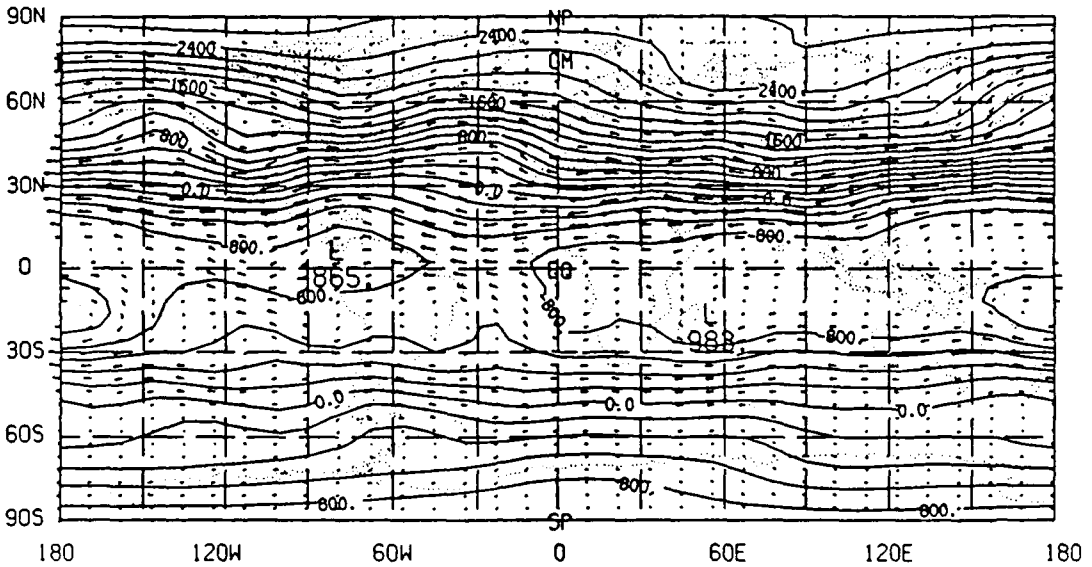

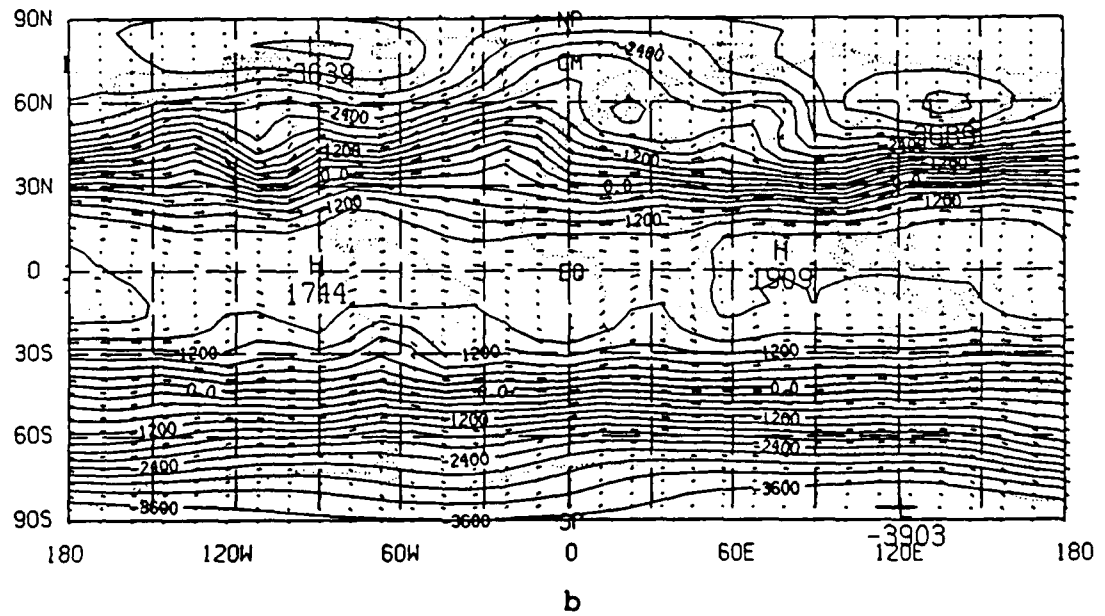

Figure 3.2. DERF period average wind vectors (m/s) with geopotential deviations from a global constant (m^2/s^2) for the internal Rossby components at (a) $\sigma = .7$ (maximum vector = 13.6 m/s; contour interval = 200 m^2/s^2) and (b) $\sigma = .3$ (maximum vector = 29.5 m/s; contour interval = 300 m^2/s^2).

Examining these same fields for the internal EG components shows important differences from the Rossby modes. A strong cross-isobaric flow is present in tropical regions, the result of the balance between the acceleration and pressure gradient force in the gravity components (Fig. 3.3). The large amplitude of the internal EG modes over extratropical mountainous regions (South America, Tibet) reflect the nongeostrophic relation between the mass and wind fields. This is probably not realistic, but only a consequence of problems with the analysis data or the vertical interpolations used to obtain the analysis data in σ surfaces. While the winds associated with the Rossby modes are strongest in mid-latitutes, the internal EG winds maximize in the tropics, reflecting the contribution of the Kelvin mode included in the EG summation. It should also be noted that there is an increase in the wind speed with height. This coupled with the reversal in wind direction at most locations between the two levels suggests that vertical mode 3 again dominates the total energy.

By examining the wind fields at $\sigma = .7$ and $\sigma = .3$, it was concluded that for both the internal Rossby and EG components, vertical mode 3 contained the most kinetic energy. The total wave energy contained in the first eight vertical modes is shown in Fig. 3.4. It must be stressed that this is energy contained in the wave component only; the average zonal wind contribution has been removed. The gravity modes show maximum total wave energy in vertical mode 4 (Fig. 3.4a). For the Rossby component (Fig. 3.4b), most of the total wave energy is found in vertical mode 3.

The DERF period average wind field at $\sigma = .7$ displays a strong westerly flow in the mid-latitudes of both the Northern and Southern Hemispheres (Fig. 3.5). The tropics have a weaker easterly flow, with maximum winds located over the central Pacific. This reflects the Walker circulation. The area of maximum standard

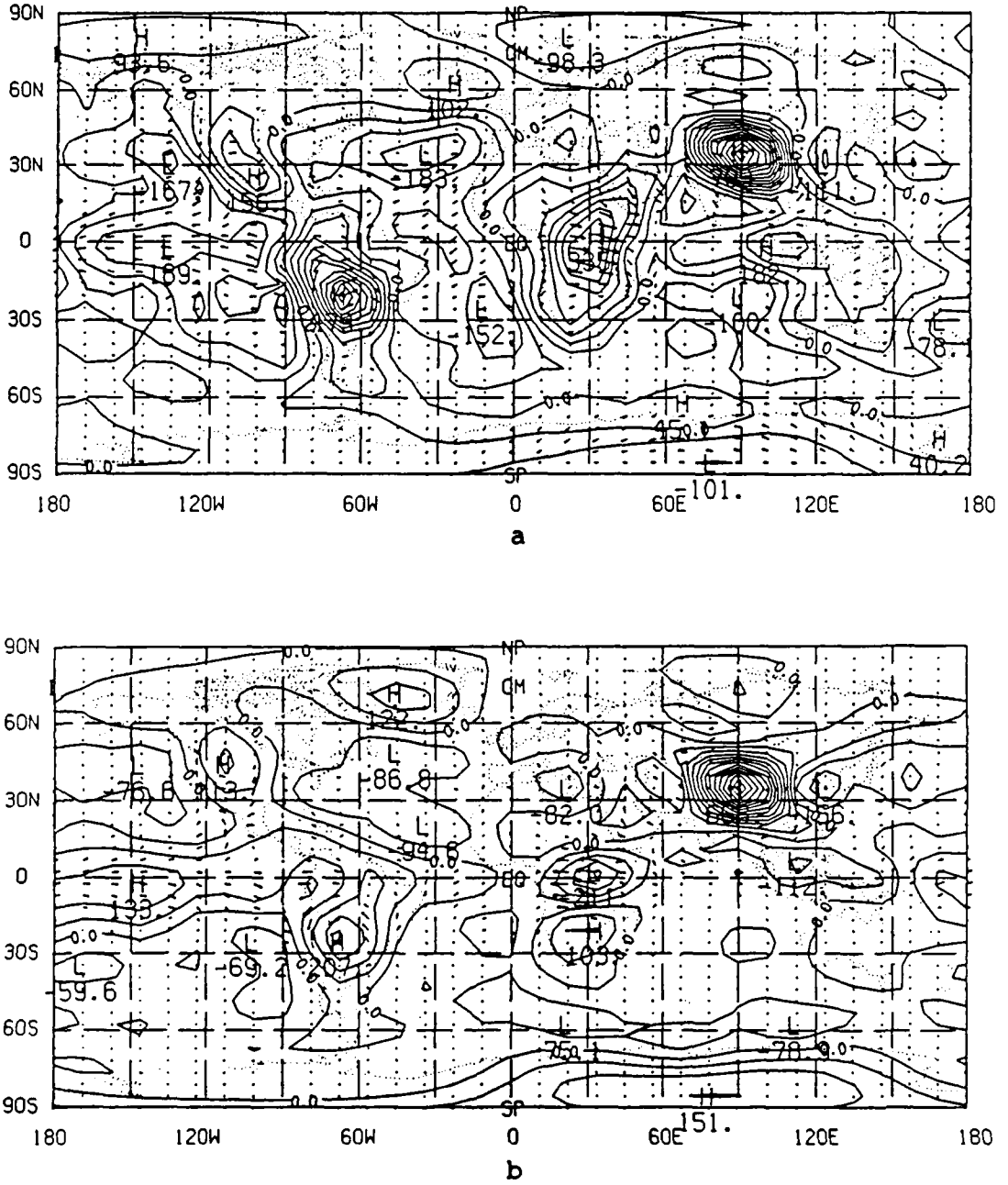

Figure 3.3. DERF period average wind vectors (m/s) with geopotential deviations from a global constant (m^2/s^2) for the internal eastward gravity components at (a) σ = .7 (maximum vector = 7.2 m/s) and (b) σ = .3 (maximum vector = 17.7 m/s). Contour interval = 50 m^2/s^2.

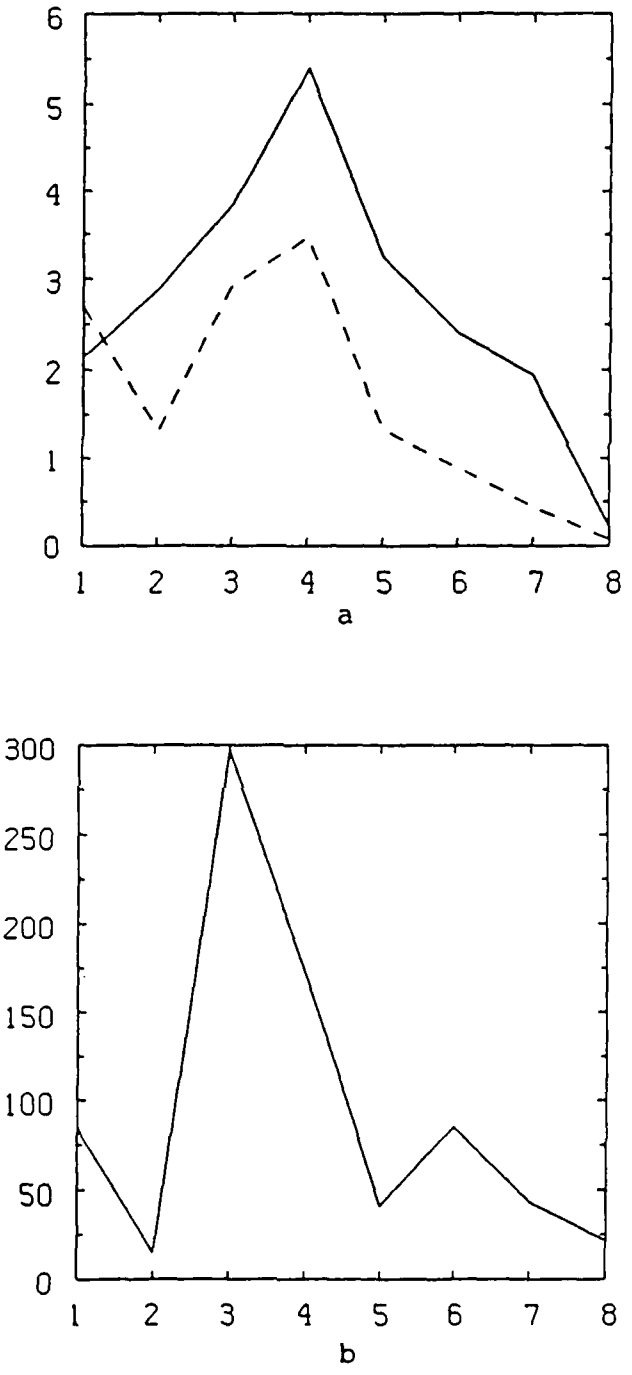

Figure 3.4. DERF period total wave energy (m^2/s^2) in the first eight vertical modes for (a) internal eastward gravity modes (solid line) and internal westward gravity modes (dashed line); (b) Rossby modes.

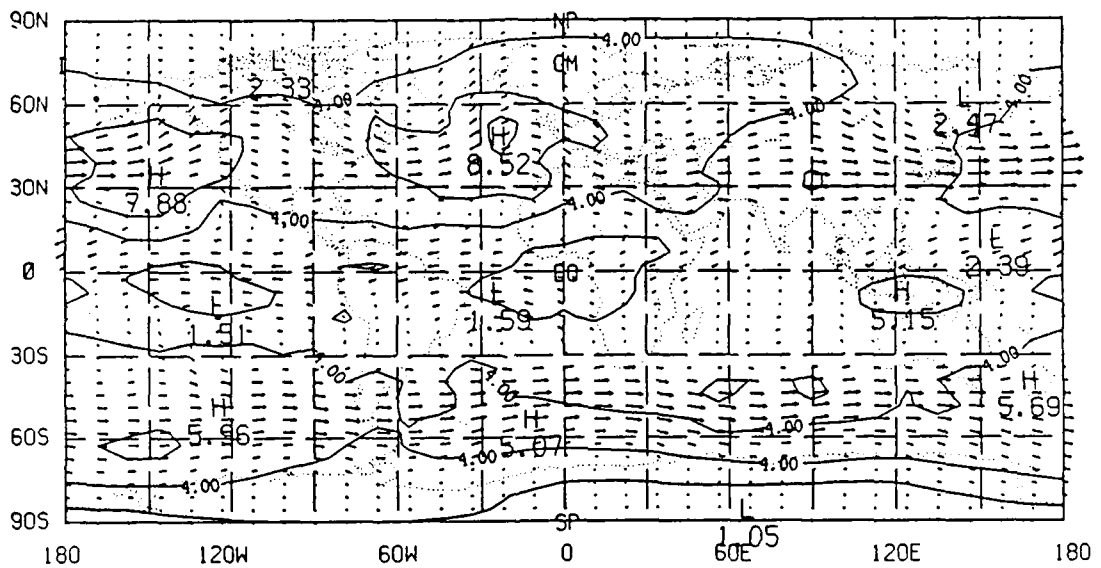

Figure 3.5. DERF period average total wind vectors (m/s) with standard deviation contoured every 2 m/s at $\sigma = .7$. The maximum vector is 18.4 m/s.

deviation is located in the Northern Hemisphere over the eastern Atlantic, where a strong blocking ridge set up at various times during the period. In fact, all the standard deviation maxima in the mid-latitudes are best seen in the external Rossby mode (not shown). While winds are relatively weak over Indonesia, a standard deviation maximum of 5.15 m/s is present over this region. This is where the 30-50 day oscillation is strongest. This signal is best seen in the internal Rossby modes (not shown).

3.3 Tropical Propagation Patterns in the Analysis Data

The 30-50 day oscillation can be identified by zonal propagation characteristics in the tropics. Figure 3.6 shows the pentad zonal wind anomalies at the tropics due to the internal EG modes. This is obtained by subtracting the DERF period average from their pentad values. Four eastward propagation cases of negative anomilies are clearly seen in this figure. The first propagation period begins at pentad 2 and circles the globe by about pentad 9. The second propagation period begins at pentad 10 and ends around pentad 14, covering only a little more than half of the globe. The next two propagation periods are much better defined and display a more rapid eastward propagation. The third case begins at pentad 15 and circles the globe by pentad 20. The last case begins at pentad 20 and shows a steady eastward propation until the end of the period. From this analysis, it is clear that the 30-50 day oscillation was quite weak during the first half of the DERF period, and much stronger during the second half.

Pentad zonal wind anomalies in the tropics due to internal Rossby modes are shown in Fig. 3.7. Their eastward propagation are not as easily discernible as for the internal gravity modes. Nevertheless, there are centers of negative anomalies moving eastward starting on pentads 2 and 15. These roughly correlate with the first

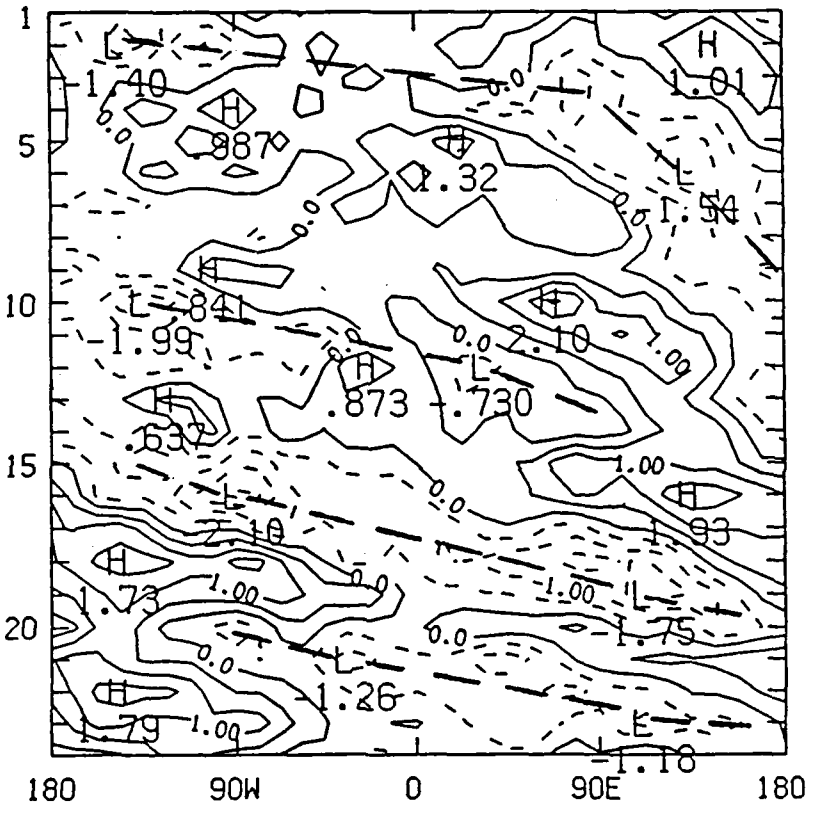

Figure 3.6. Pentad vs. longitude diagram of zonal wind anomalies (m/s) in the tropics (20° N - 20° S) for the internal eastward gravity modes at σ = .7. Dashed lines indicate subjectively determined movement of low centers. Contour interval = 0.5 m/s.

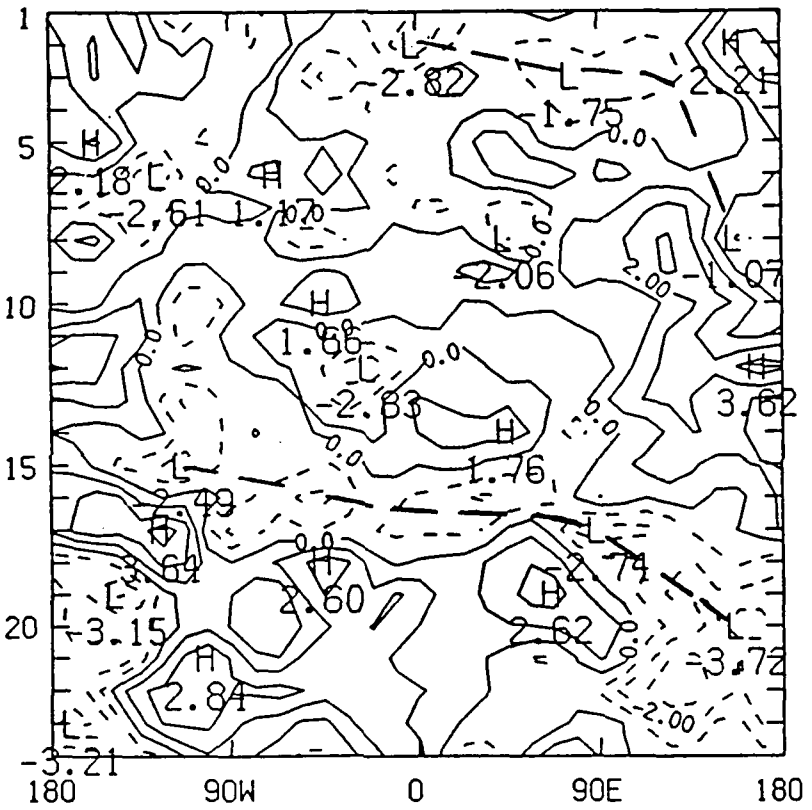

Figure 3.7 Pentad vs. longitude diagram of zonal wind anomalies (m/s) in the tropics (20° N - 20° S) for the internal Rossby modes at $\sigma = .7$. Dashed lines indicate subjectively determined movement of low centers. Contour interval = 1.0 m/s.

and third cases seen in the internal EG case. Additionally, an eastward propagation of positive anomaly centers starts around pentad 16 and ends at pentad 21.

Pentad anomalies in the tropics for total rainfall and surface latent heat flux are seen in Fig. 3.8 and Fig. 3.9, respectively. Although the overall signal is not that clear, centers of positive total rainfall anomilies appear to be moving eastward beginning on pentad 3 (80° E) and continue through pentad 14 (180° E). Weak negative surface latent heat anomalies, indicating stronger upward fluxes than those for the DERF average, follow this same basic pattern. These propagation patterns roughly correspond to the first propagation case noted in the internal EG case (see Fig. 3.7). A second eastward propagation pattern of positive total rain anomalies begins at pentad 16 (160° W) and continues until the end of the period (45° E). While this pattern does match up exactly with the third or the fourth propagation cases seen in the EG case, it could be a reflection of either or both of these. It is interesting to note that easterly anomalies are associated with upward anomaly fluxes from 90° E to the date line, in agreement with the theories of Emanuel (1987) and Neelin et al. (1987).

The analysis of outgoing longwave radiation (OLR) data from an independent source shows that propagation patterns of negative OLR anomalies (not shown) match up very well with the positive anomaly patterns seen in the total rainfall. The OLR is quite sensitive to cloud-top temperatures, and delineates the long-term variations of tropical convection better than other existing conventional measurements (Lau and Chan, 1985).

In summary, clear reflections of the 30-50 day oscillation can be seen in both the internal eastward gravity and the internal Rossby modes. The goal of this investigation is to compare forecasts when the signature of the oscillation is strong with those when it is quite weak. Cases must be selected for each of these sit-

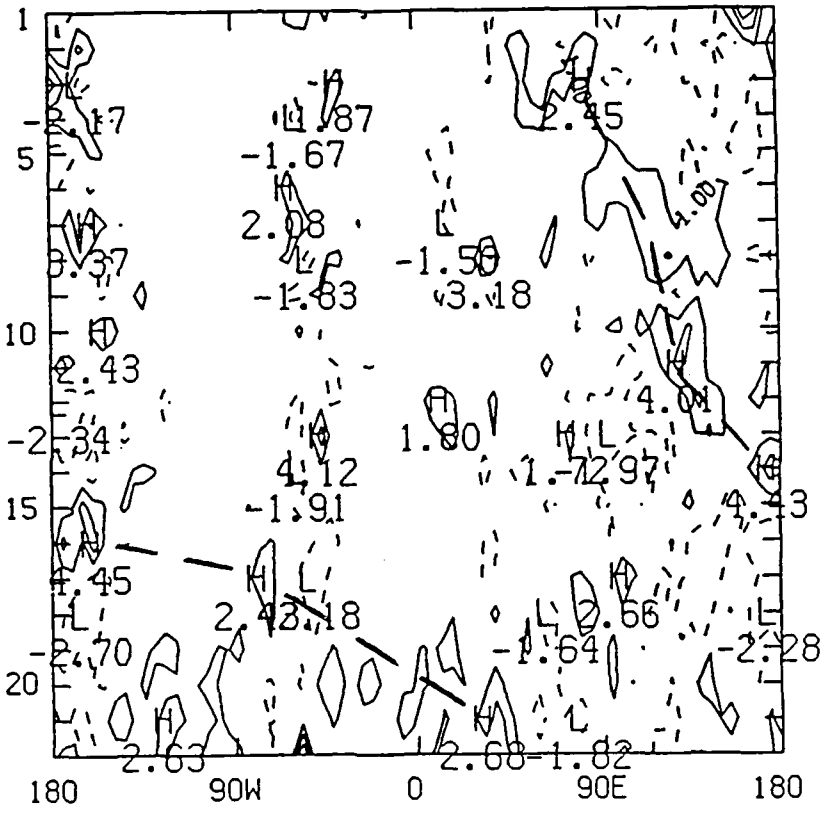

Figure 3.8. Pentad vs. longitude diagram of total rainfall anomalies (mm/day) in the tropics (20° N - 20° S). Dashed lines indicate subjectively determined movement of high centers. Contour interval = 2.0 mm/day.

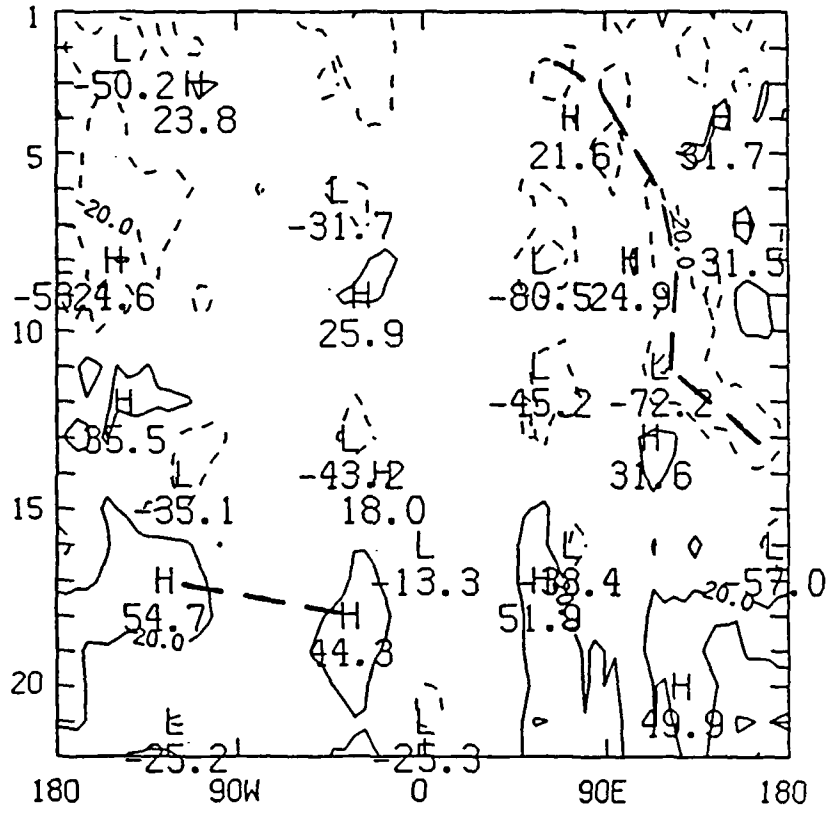

Figure 3.9. Pentad vs.. longitude diagram of surface latent heat flux anomalies (W/m^2) for the tropics (20° N - 20° S). Dashed lines indicate subjectively determined movement of low/high centers. Contour interval = 40 W/m^2.

uations. Comparison cases are based on Fig. 3.6, which exhibits the most clear signature of the intraseasonal oscillation. In the internal eastward gravity modes, there are four propagation periods, beginning on pentads 2, 10, 15, and 20 (see Fig. 3.6). The first two cases are slow and poorly defined, while the last two display a strong signature and rapid eastward propagation. The second case, which begins on pentad 10, cannot be examined because forecast data are missing for one of the days (31 January). Additionally, the final case, which starts on pentad 20, can not be scrutinized because the analysis data only extends to 6 April while the forecast data goes out to 11 April. Therefore, by process of elimination, the case selection has been made. The example of when the oscillation is weak and slow moving is designated as Case A. It begins at pentad 2 (17 Dec 86), and requires eight pentads to circle the globe, finishing on pentad 9 (21 Jan 87). The case of a strong, rapidly moving oscillation is Case B. It begins on pentad 15 (20 Feb 87), and makes one complete propagation around the globe in only five pentads, finishing on pentad 19 (12 Mar 87).

3.4 Contrasts Between the Oscillation Cases

In this section, a comparison will be made between the two cases defined earlier. The analysis data of four meteorological parameters will be examined: heights, total rainfall, surface latent heat flux, and surface sensible heat flux.

The 700 mb height fields for both Case A and Case B are shown in Fig. 3.10. Case A has a better defined height field in the Northern Hemisphere, indicating a stronger overall zonal flow. It also has two strong ridges, one over the western United States and another over the extreme eastern Atlantic. Case B has much weaker ridging in these areas, but a strong blocking low off the east coast of Canada is present. This was only a weak trough during Case A. The Southern Hemisphere

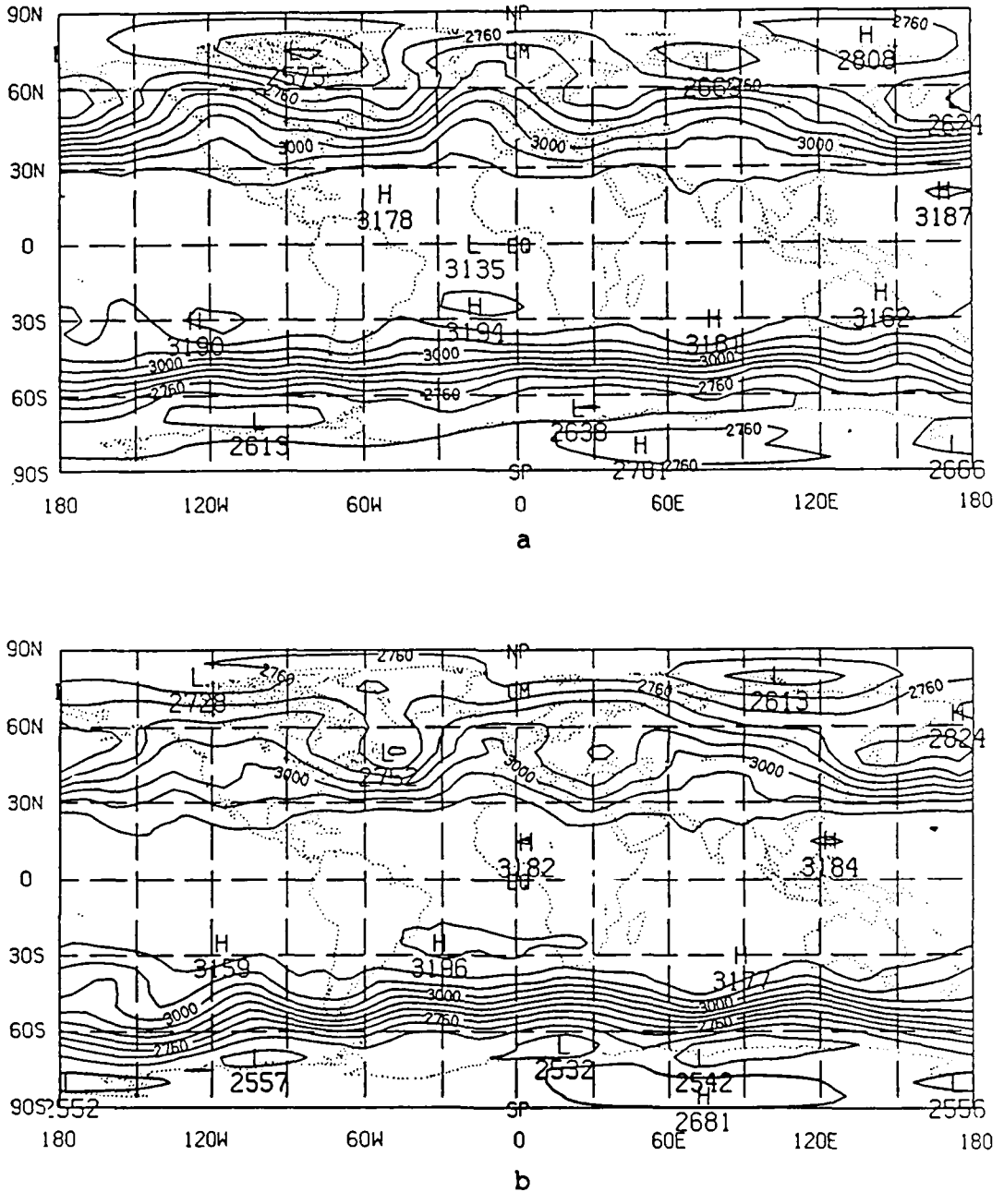

Figure 3.10. Average 700 mb heights (m) for (a) Case A and (b) Case B. Contour interval = 60 m.

mid-latitudes are more zonal in both cases, with larger amplitude stationary waves over the Pacific Ocean in Case B.

To examine the height field differences between these cases, the Case A heights are subtracted from the Case B heights for both 700 mb and 300 mb (Fig. 3.11). A large difference exists over Canada at both levels. Because this difference does not change position and increases only slightly with height, it is barotropic in nature, and contained mainly in vertical mode 1. The differences in the Southern Hemisphere are basically stationary; however, they increase dramatically with height. These differences are more baroclinic, and manifest themselves in vertical mode 3. The large difference over the Soviet Union moves slightly westward and increases dramatically with height. This is also baroclinic. This further illustrates how the modal breakdown gives special insights into the situation.

The DERF period average total rainfall (Fig. 3.12) shows that as expected, the majority of the rainfall is located in the tropics, generally just south of the equator (in the summer hemisphere). The areas of maximum rainfall are over New Guinea, the tropical central Pacific, Brazil, and along the southeast coast of Africa. The differences between the Case A and Case B total rainfall (B minus A) are shown in Fig. 3.13. The largest differences occur in Peru (+7.70 mm/day), the Indian Ocean (+7.23 mm/day), and the equatorial central Pacific near the date line (5.78 mm/day). All of these differences are the result of heavier rainfall during Case B, when the oscillation was well-defined.

The largest DERF period average surface latent heat fluxes should occur in areas of greatest evaporation. Figure 3.14 shows that this is the case. There are large negative fluxes along the east coasts of North America and Asia; in each location there is a warm ocean current that adds to the evaporative process. Other large fluxes are located over the Arabian Sea and New Guinea. The New Guinea

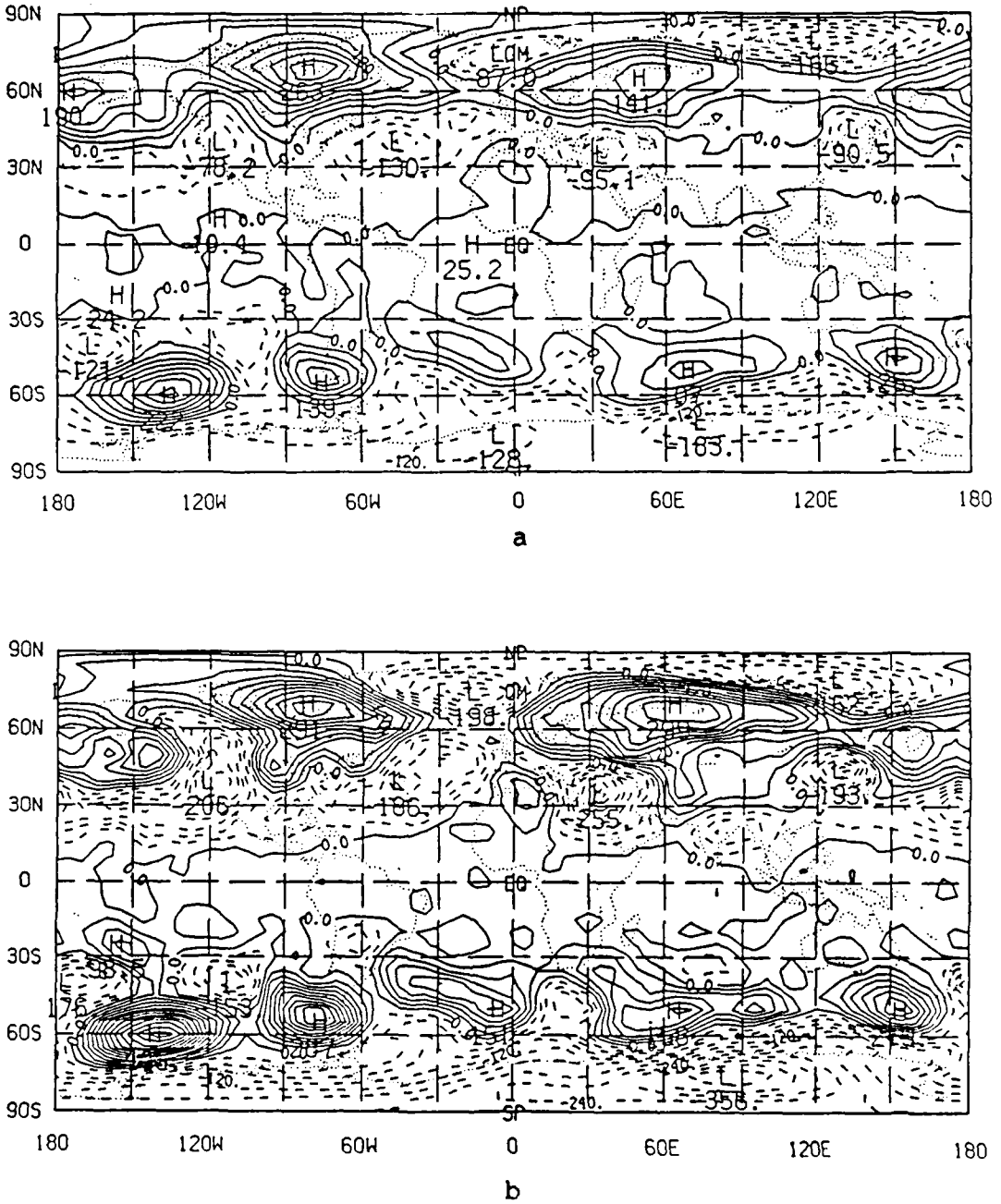

Figure 3.11. Case B minus Case A average heights (m) for (a) 700 mb and (b) 300 mb. Contour interval = 30 m.

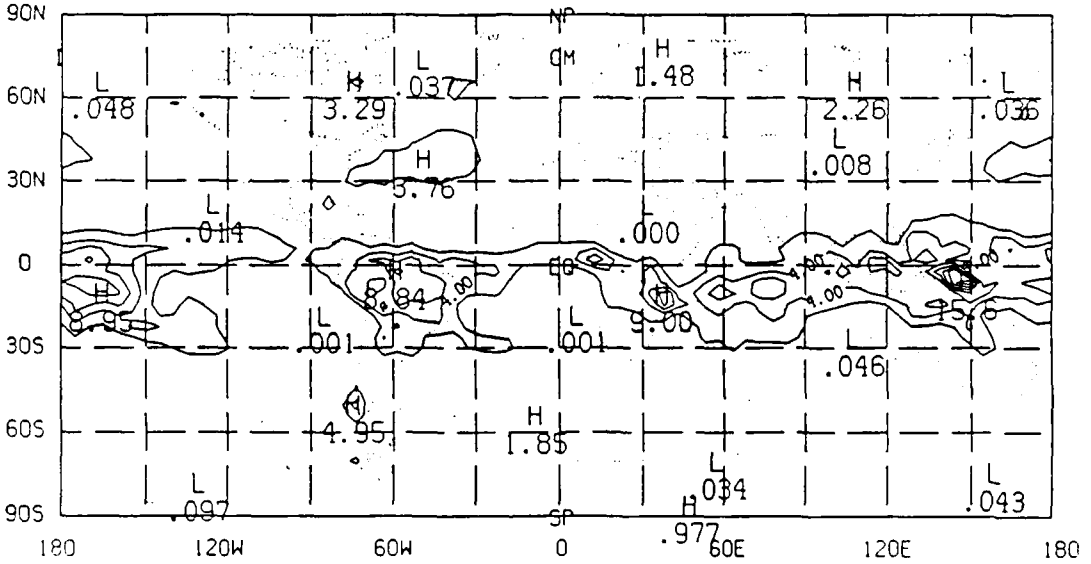

Figure 3.12. DERF period average total rainfall (mm/day). Contour interval = 2 mm/day.

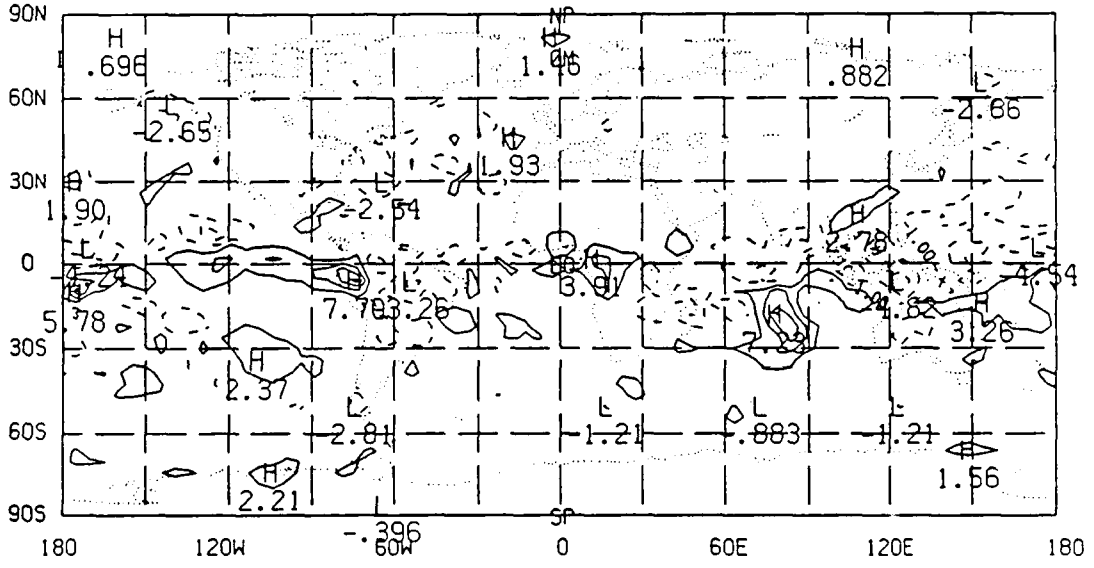

Figure 3.13. Case B minus Case A average total rainfall (mm/day). Contour interval = 2 mm/day.

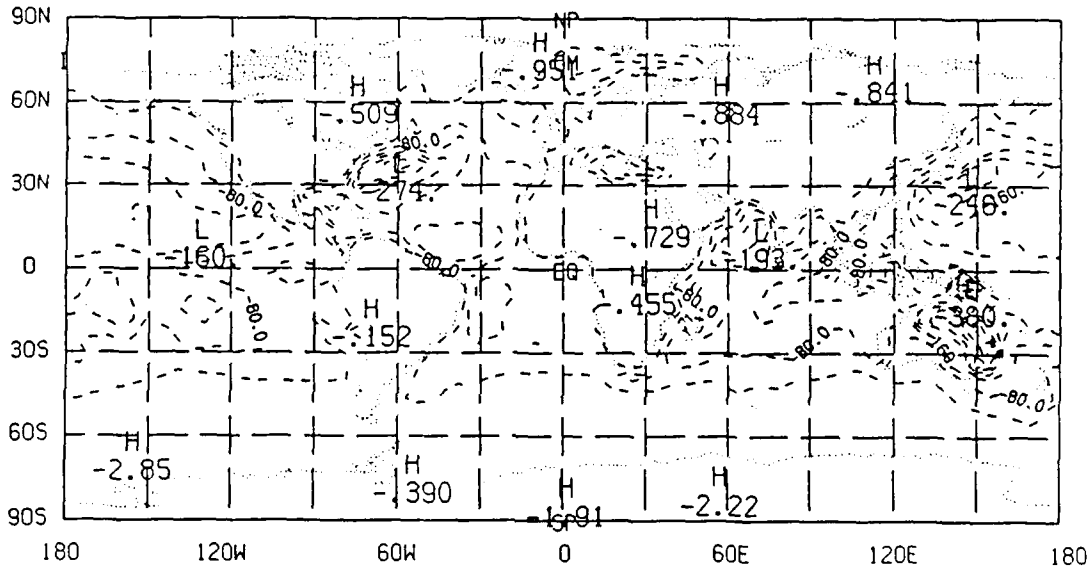

Figure 3.14. DERF period average surface latent heat flux (W/m^2). Contour interval = 40 W/m^2.

flux corresponds very closely with the area of maximum total rainfall during the DERF period. Of special note is the maximum flux over northeastern Australia. This appears to be an error in the analysis data, as evaporation in this area would be at a minimum. The differences between the Case A and Case B surface latent heat flux (B minus A) is shown in Fig. 3.15. The area of greatest difference is in the Arabian Sea (+129 W/m^2). Case A has a very large negative flux in this region, while the Case B flux is much smaller. Additionally, the flux off the Asian coast is much larger in Case A than in Case B. Differences in this region reach +128 W/m^2. Large positive differences also occur in the central and eastern Pacific. Generally, it can be stated that the Case A surface latent heat fluxes are larger than that observed in Case B.

Like the surface latent heat flux, the DERF period average surface sensible heat flux shows maximum negative fluxes along the east coasts of North America and Asia (Fig. 3.16). Once again a questionable maximum flux is found over northeastern Australia. Another large flux is located over the Barents Sea, north of the Soviet Union. These maximums are much smaller than those found in the surface latent heat flux, possibly related to excessive evaporation. The largest difference between the two cases (B minus A) is located over the extreme North Atlanic, near Grenwich mean (Fig. 3.17). This is the result of Case B having a very large negative flux in this region. Another major difference occurs long the Asian coast, the result of very large negative fluxes in Case A. The sensible heat flux fields do not appear to provide any new insight in the description of the intraseasonal oscillation, and will not be considered any further.

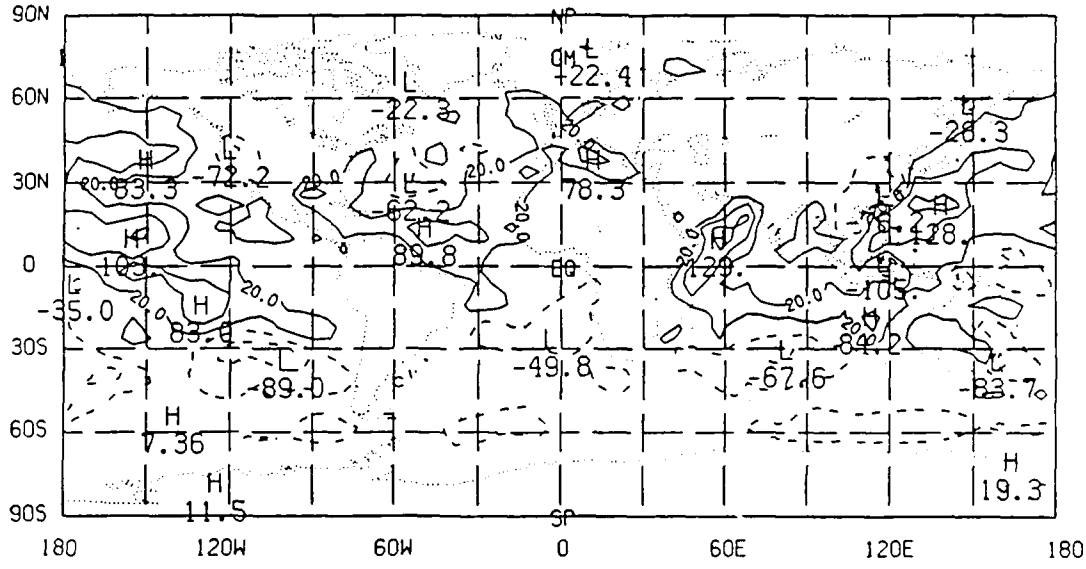

Figure 3.15. Case B minus Case A average surface latent heat flux (W/m^2). Contour interval = 40 W/m^2.

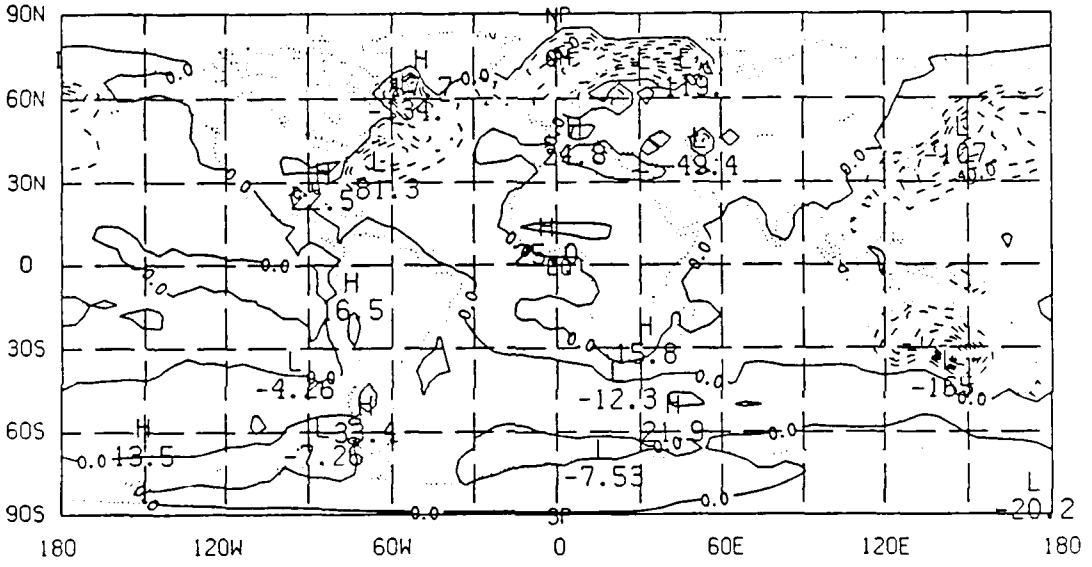

Figure 3.16. DERF period average surface sensible heat flux (W/m^2). Contour interval = 20 W/m^2.

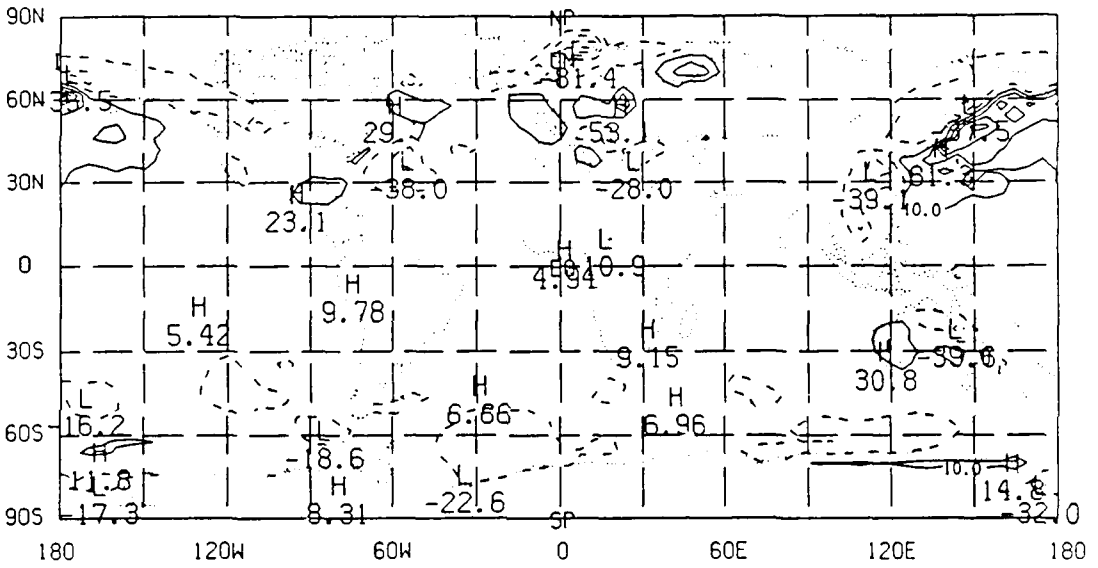

Figure 3.17. Case B minus Case A average surface sensible heat flux (W/m^2). Contour interval = 20 W/m^2.

CHAPTER 4

PREDICTABILITY

4.1 Introduction

The DERF period analysis data were studied in the last chapter. The strongest and most clear signature of the 30-50 day oscillation was discovered in the tropical zonal wind anomalies. The quality of the forecasts during this period will now be examined for when the oscillation was strong (Case B) and when it was weak (Case A). Section 4.2 will evaluate the model's ability to forecast the basic signature of the oscillation. In Section 4.3, errors in the 700 mb wind field will be addressed. These error fields will then be decomposed into different horizontal modes in Section 4.4. Section 4.5 will identify propagation patterns in the error fields which display interactions between the tropics and extratropics. Lastly, Section 4.6 will show errors in the total rainfall field.

4.2 Forecasted Propagation of the 30-50 Day Oscillation

It was shown in Chapter 3 that the 30-50 day oscillation is best identified by internal EG zonal wind anomalies in the tropics. Figure 3.6 showed four cases of eastward propagating negative anomalies, which is the signature of the oscillation. This section addresses the question of how well the forecast model reflects this signature. The forecasted internal EG zonal wind anomalies in the tropics at $\sigma = .7$ are shown in Fig. 4.1 for Case A. They were obtained by subtracting the DERF period average zonal wind from the forecasted pentad value. The eight separate

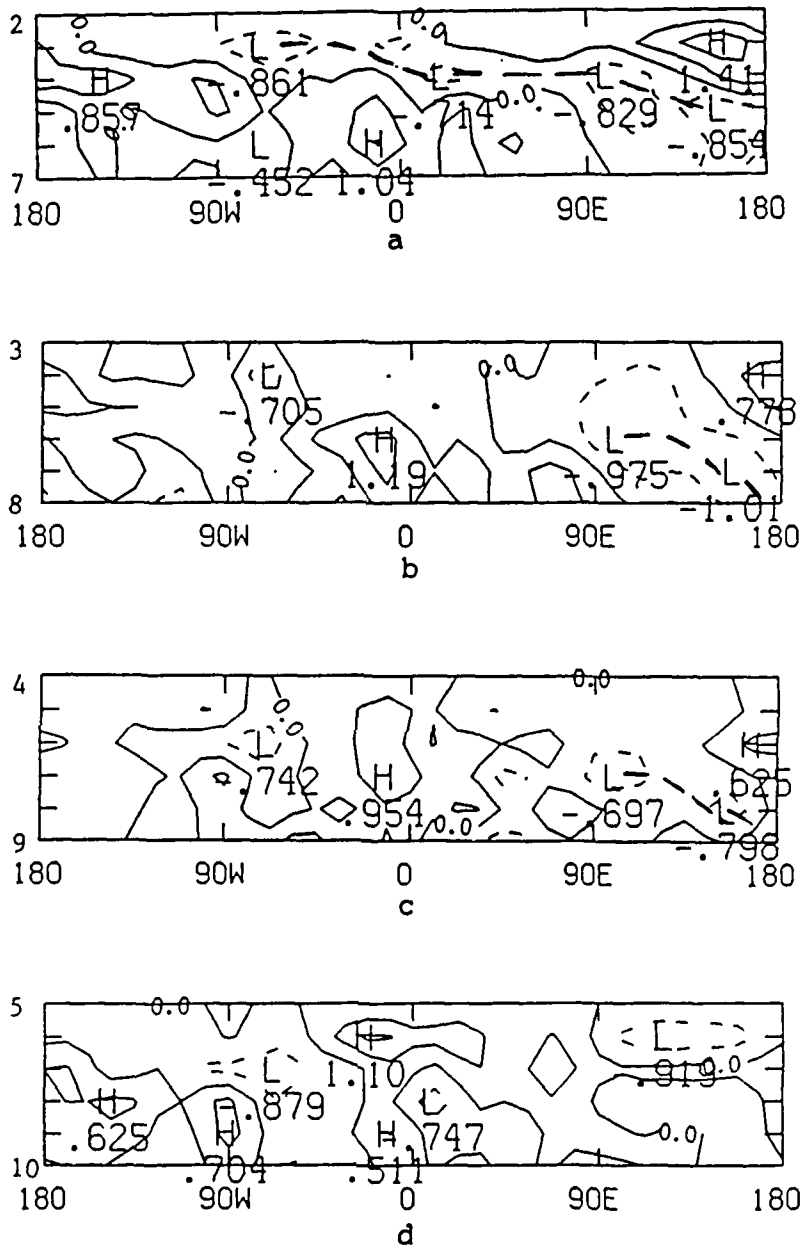

Figure 4.1. Pentad vs. longitude diagrams of forecasted zonal wind anomalies (m/s) in the tropics (20° N - 20° S) for the internal eastward gravity modes at σ = .7. This contains the eight forecasts from Case A (a-h), covering the time period from 17 Dec 86 (pentad 2) to 15 Feb 87 (pentad 14). Dashed lines indicate subjectively determined movement of low centers. Contour interval = 0.5 m/s.

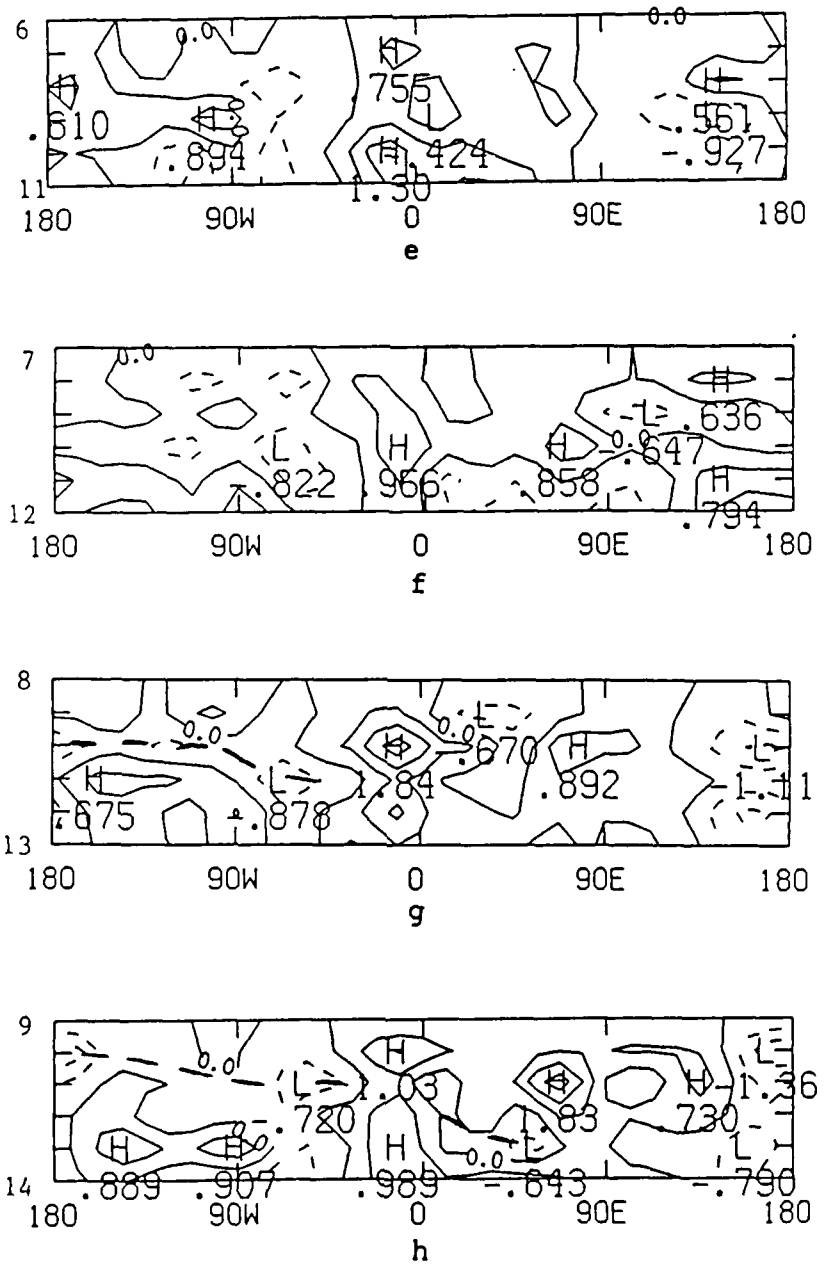

Figure 4.1. (continued).

forecasts contained in Case A are shown individually to point out the ability of the forecast to reproduce the signature of the oscillation for each realization. Comparing these forecasts to Fig. 3.6, it is obvious that the first propagation period is handled fairly well by the forecasts. The forecast beginning on pentad 2 (Fig. 4.1a) shows a well-defined eastward propagation from about 80° W to 180° E. The forecasts beginning on pentad 3 and 4 continue to show the negative anomaly propagating between 90° E and the date line. In Fig. 4.1g, the first reflection of the second propagation case can be seen, from pentad 10 (180°) to pentad 11 (70° W). This, however, is much weaker than the signal seen in the analysis. The forecast starting on pentad 9 (Fig. 4.1h) continues to show this propagation, and extends it further east, to about 60° E by pentad 13. It also shows an area of positive anomalies interrupting this propagation near the equator. This is actually very close to the pattern seen in the analysis.

The five separate forecasts contained in Case B are in Fig. 4.2. The forecast beginning on pentad 15 (Fig. 4.2a) shows a weak reflection of the eastward propagating negative anomaly beginning around 90° W and continuing to the date line by pentad 18. The next forecast (Fig. 4.2b) continues to show this propagation pattern. The forecast beginning on pentad 17 (Fig. 4.2c) has some very interesting results. The propagation pattern is seen from about the equator eastward. However, the forecast appears to be slower than what the analysis indicates. By pentad 21 the forecast has the negative anomaly center at around 110° E, while the analysis has it to the date line (180° E). This is different from what has been found in other general circulation models (e.g., Hayashi and Sumi, 1986), where the speed of the oscillation is greater than that observed in nature. Also of note in this forecast is the strong positive anomaly present at pentad 18 (150° W). A very similar pattern is seen in the analysis. The final two forecasts, beginning on pentads 18 and 19,

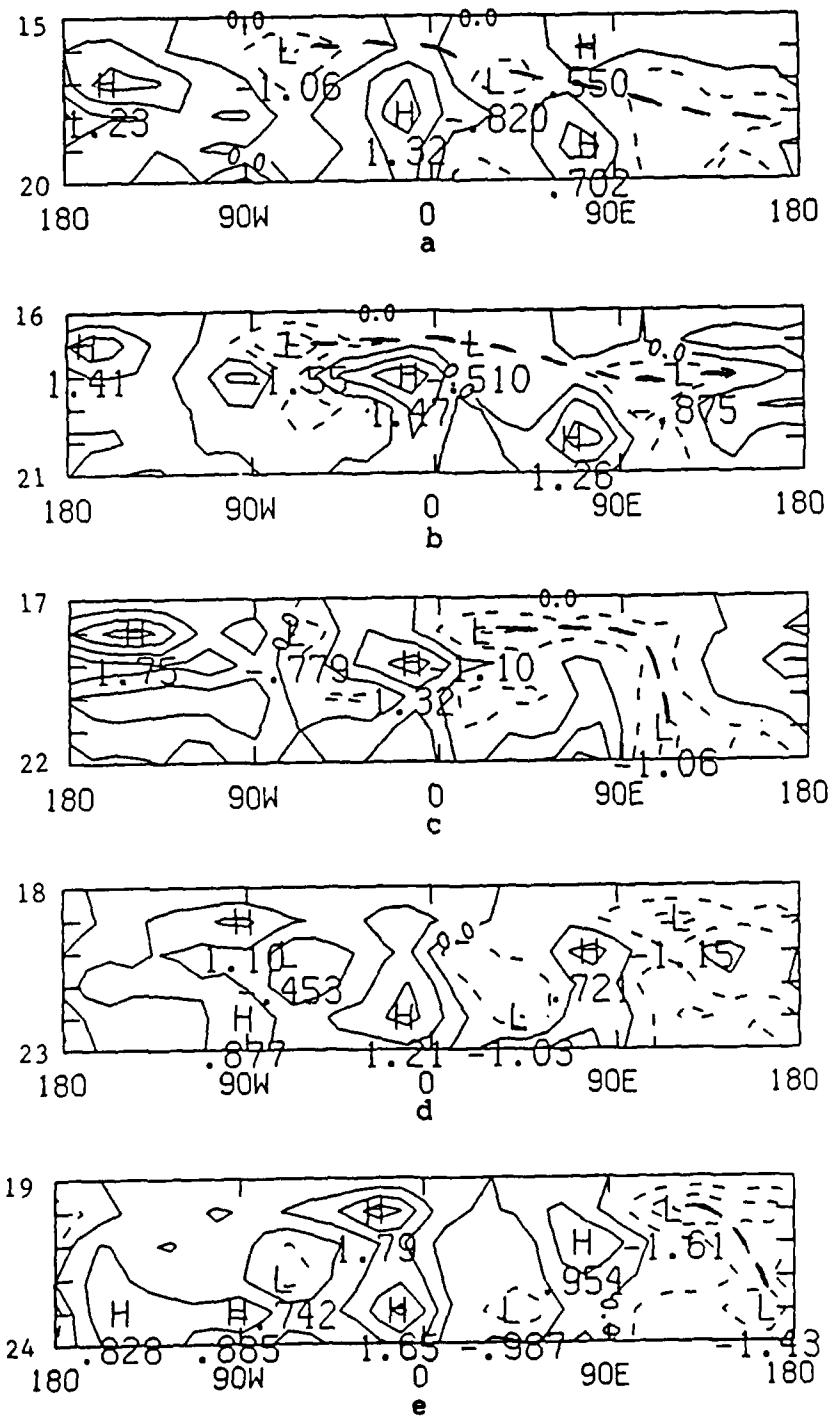

Figure 4.2. Pentad vs. longitude diagrams of forecasted zonal wind anomalies (m/s) in the tropics (20° N - 20° S) for the internal eastward gravity modes at σ = .7. This contains the five forecasts from Case B (a-e), covering the time period from 20 Feb 87 (pentad 15) to 6 Apr 87 (pentad 24). Dashed lines indicate subjectively determined movement of low centers. Contour interval = 0.5 m/s.

fail to show any real indication of the fourth propagation pattern seen in the analysis. They also show strong positive anomalies around Grenwich mean, which is not present in the analysis.

In summary, the reflection of the 30-50 day oscillation present in tropical zonal wind anamolies can be seen in forecasts when the oscillation is both strong and weak. The forecasted signature of the oscillation is usually much weaker than what the analysis indicates. Generally speaking, it can be concluded that the model tends to forecast the propagation of this phenomenon slightly better when it is weak (Case A). This may be because it propagates slower during this time.

4.3 Errors in the 700mb Wind

How well the forecast model handles the 700 mb wind field is shown in Fig. 4.3. This figure contains the average RMS difference for days 1 through 15 along with the running 5-day mean for both Case A and Case B in the Northern Hemisphere (20° N - 80° N), the Southern Hemisphere (20° S - 80° S), and the tropics (20° N - 20° S). As expected, the averaging process does improve the quality of the forecasts in all cases.

Tracton et al. (1989) found that the model output degrades significantly during the evolution of blocking circulations. This explains why the forecast in the Northern Hemisphere is inferior during Case A, and the forecast in the Southern Hemisphere is inferior during Case B. The average 700 mb height field for Case A shows a large blocking ridge over the extreme eastern Atlantic, just off the Europeon coast, while the Southern Hemisphere has a mostly zonal flow (see Fig. 3.10a). During Case B, the height field shows the development of stationary high amplitude waves over the central and eastern Pacific of the Southern Hemisphere, while the blocking patterns in the Northern Hemisphere are much weaker than they

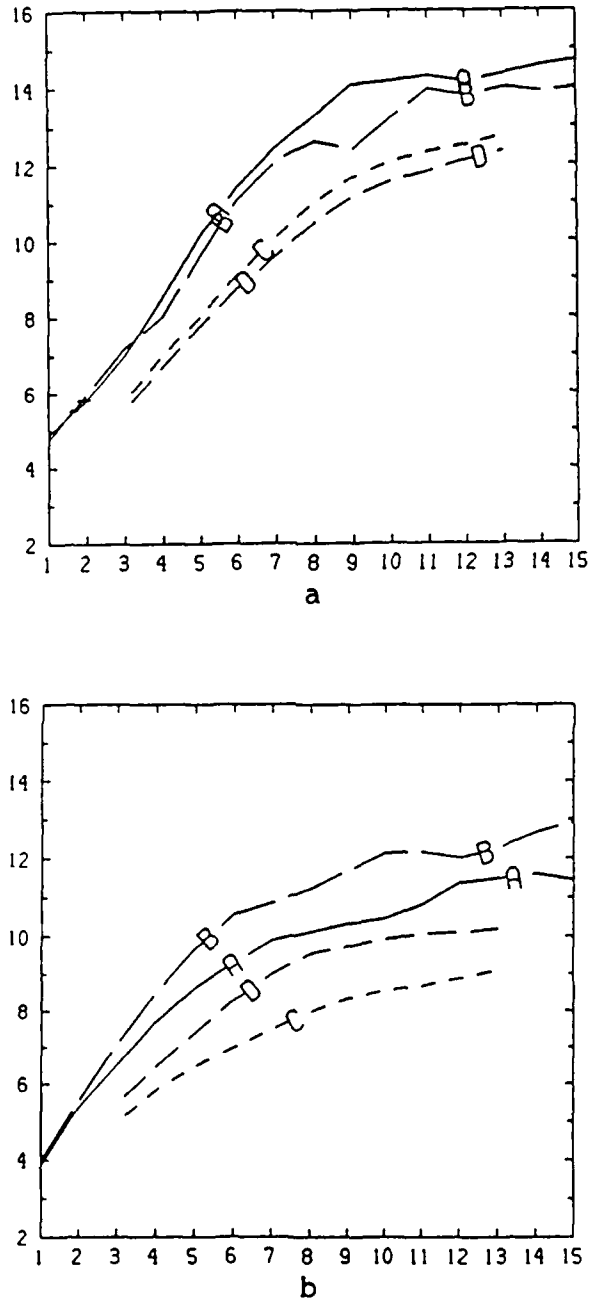

Figure 4.3 Average RMS difference (m/s) of the 700 mb wind for forecast days 1 through 15 (line A: Case A, line B: Case B) and the running 5-day mean (line C: Case A, line D: Case B) for the (a) Northern Hemisphere (20° N - 80° N), (b) Southern Hemisphere (20° S - 80° S), and (c) tropics (20° N - 20° S).

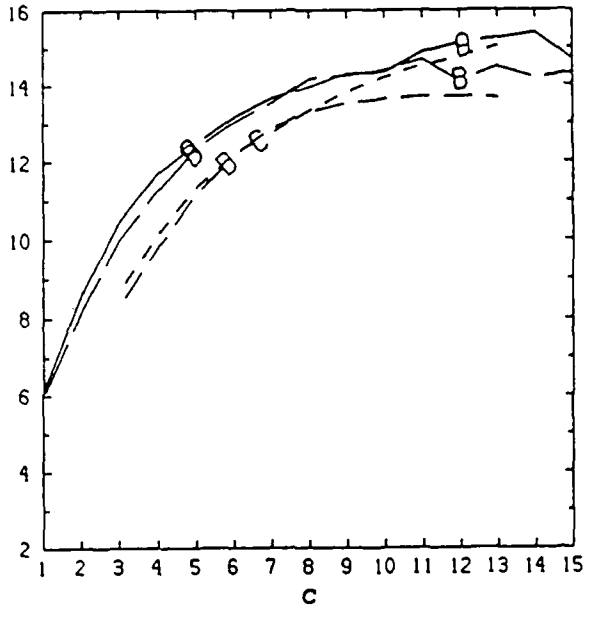

Figure 4.3 (continued).

were during Case A (see Fig.3.10b). This is also reflected on the skill of persistance in the Northern Hemisphere, which Tracton et al. (1989) showed to be considerably greater for Case A than for Case B.

The error pattern for the tropical 700 mb wind is shown in Fig 4.3c. The wind field in the tropics is much different than that in mid-latitudes. While there is a strong rotational component, there is also a sizable divergent component produced by forced motion (diabatic heating). Kelvin modes dominate this motion; they are trapped in the tropics and have almost no meridional velocity. To better understand the nature of the errors as well as tropical/extratropical interactions, the wind field error will be decomposed into rotational and divergent modes.

4.4 Modal Breakdown of Wind Errors

Predictability curves for the mostly rotational (Rossby) and divergent (inertia-gravity) modes will now be presented. The zonally averaged RMS difference is computed for the magnitude of the wind vector at $\sigma = .7$. Next, the values obtained for each latitude are summed over the Northern Hemisphere, Southern Hemisphere, and the tropics to obtain a total RMS difference for these regions.

Errors in the tropics are shown in Fig. 4.4. The EG contributions (contained mainly in the Kelvin modes) show a much greater error in Case B. The error in the internal Rossby modes is more than twice as much as the EG components. Additionally, the Case B error is larger in this mode. Even though the magnitude of the wind in the external Rossby modes (tropics) is less than that in the internal Rossby modes, the error in the wind field is quite pronounced. Reasons for this will be discussed later.

Divergent motions are small for large-scale extratropical flow, so only errors in rotational flow components will be considered for these regions (Fig. 4.5). The

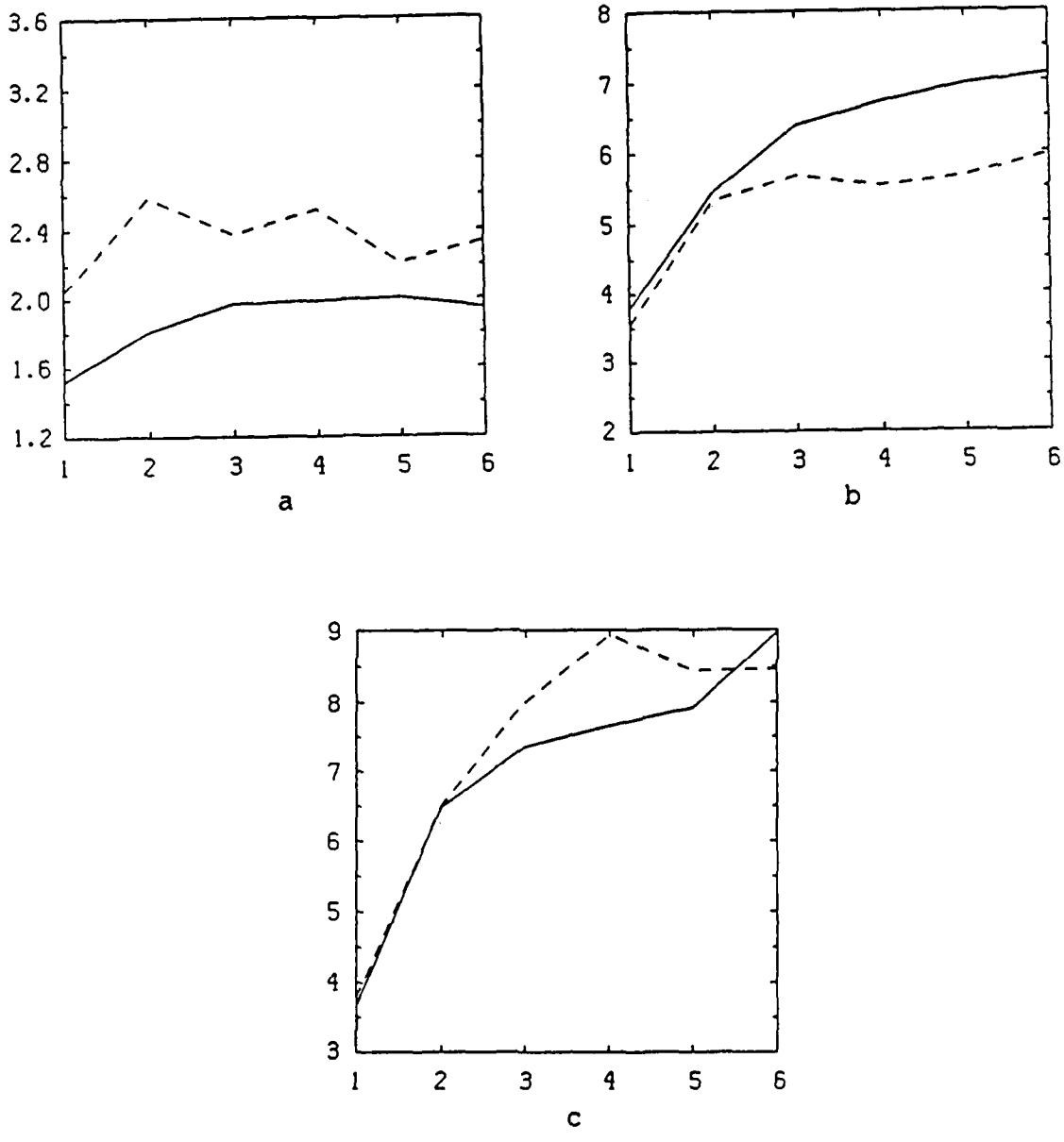

Figure 4.4. Zonally averaged RMS difference (m/s) of the $\sigma = .7$ wind over 6 pentads (abscissa) in the tropics (20° N - 20° S) for (a) internal eastward gravity modes, (b) internal Rossby modes, and (c) external Rossby modes. Solid lines = Case A and dashed lines = Case B.

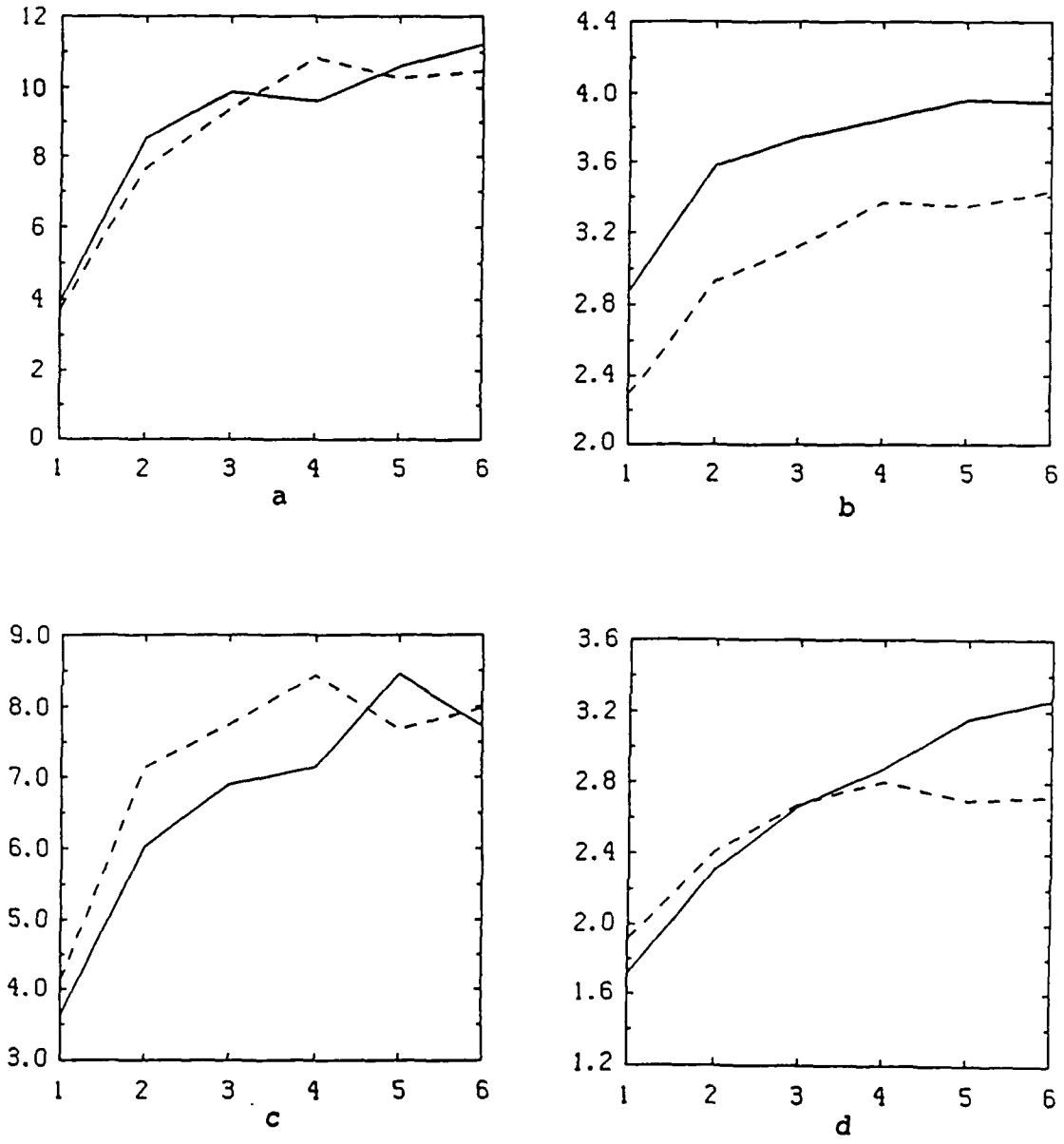

Figure 4.5. Zonally averaged RMS difference (m/s) of the σ = .7 wind over 6 pentads (abscissa) in the Northern Hemisphere (20° N - 80° S) for (a) external Rossby modes and (b) internal Rossby modes; in the Southern Hemisphere (20° S - 80° S) for (c) external Rossby modes and (d) internal Rossby modes. Solid lines = Case A and dashed lines = Case B.

errors found in the external Rossby modes are more than twice as large as those found in the internal Rossby modes. This is because most of the mid-latitude flow is contained in the external Rossby modes. In the Northern Hemisphere, the error curves for cases A and B are very similar in this mode. While the error in the internal Rossby modes is much smaller, there is a noticable difference between cases A and B. The forecast in Case A is significantly worse. This is probably the result of the strong high amplitude blocking pattern over the eastern Atlantic during Case A. In the Southern Hemisphere, the Case B error in the external Rossby mode is generally higher than that found in Case A. Again, this may be due to the development of stationary high amplitude waves in the southern Pacific during Case B. In the internal Rossby modes, the Case B error is slightly larger early in the forecast period, while the Case A error becomes substantially larger by pentad 6 for the Southern Hemisphere flow.

Ferranti et al. (1990) investigated tropical/extratropical interactions in extended range forecasts. They found that when the extratropical forecasts are relaxed towards the analysis, the impact in the tropics is more pronounced on the nondivergent flow than on the divergent flow. The forecast of the rotational flow in the tropics is greatly improved, while only a small improvement is seen in the divergent component. When the tropics are relaxed towards the analysis, improvements are seen in the extratropical forecasts of the Northern Hemisphere. It is interesting to note that compared to the Pacific and Asian areas, they found that the Atlantic region was not as susceptible to improvements in the tropical forecasts.

With this in mind, the rotational errors in the Northern Hemisphere and the tropics will be compared. In the internal Rossby modes, the error curves are quite similar, with the Case A error consistently larger than Case B (see Figs. 4.4b and 4.5b). There are also striking similarities between the external Rossby error profiles

(Figs. 4.4c and 4.5a). In both locations there is a sharp error increase in Case B at pentad 4. The Case B error then becomes less than the Case A error by pentad 6. Thus, in the rotational modes, the tropical error appears to have the same behavior as the error pattern in the Northern Hemisphere. To get a better understanding of this apparent tropical/extratropical interaction, a graphic representation of these error patterns will be presented, in an attempt to see error propagation between different parts of the globe.

4.5 Tropical/Extratropical Interactions

Figures 4.6 and 4.7 show the average 700 mb zonal wind error (*forecast minus* analysis) for the first three pentads of Case A and Case B, respectively. The error is basically stationary for both cases. In Case A, a very large error develops in the Northern Hemisphere over the eastern Atlantic. This is a reflection of the large blocking ridge discussed earlier (see Fig 3.10a). The forecast in the Southern Hemisphere is superior to that of the Northern Hemisphere, because the flow is more zonal. In Case B, a large stationary error develops in the Southern Hemisphere over the central Pacific (near date line), due to high amplitude waves in this region. Stationary errors also develop over the Soviet Union and along the North American coast during this time. These are due to well-defined stationary troughs (see Fig. 3.10b).

The relationship between the extratropical and tropical wind errors will be examined next. This is better seen by considering differences in the error field from one pentad to another. More specifically, do these differences propagate, and in which horizontal modes do they propagate?

The RMS differences presented in the previous section suggest that rotational motions in the extratropics (especially the Northern Hemisphere) influence tropical

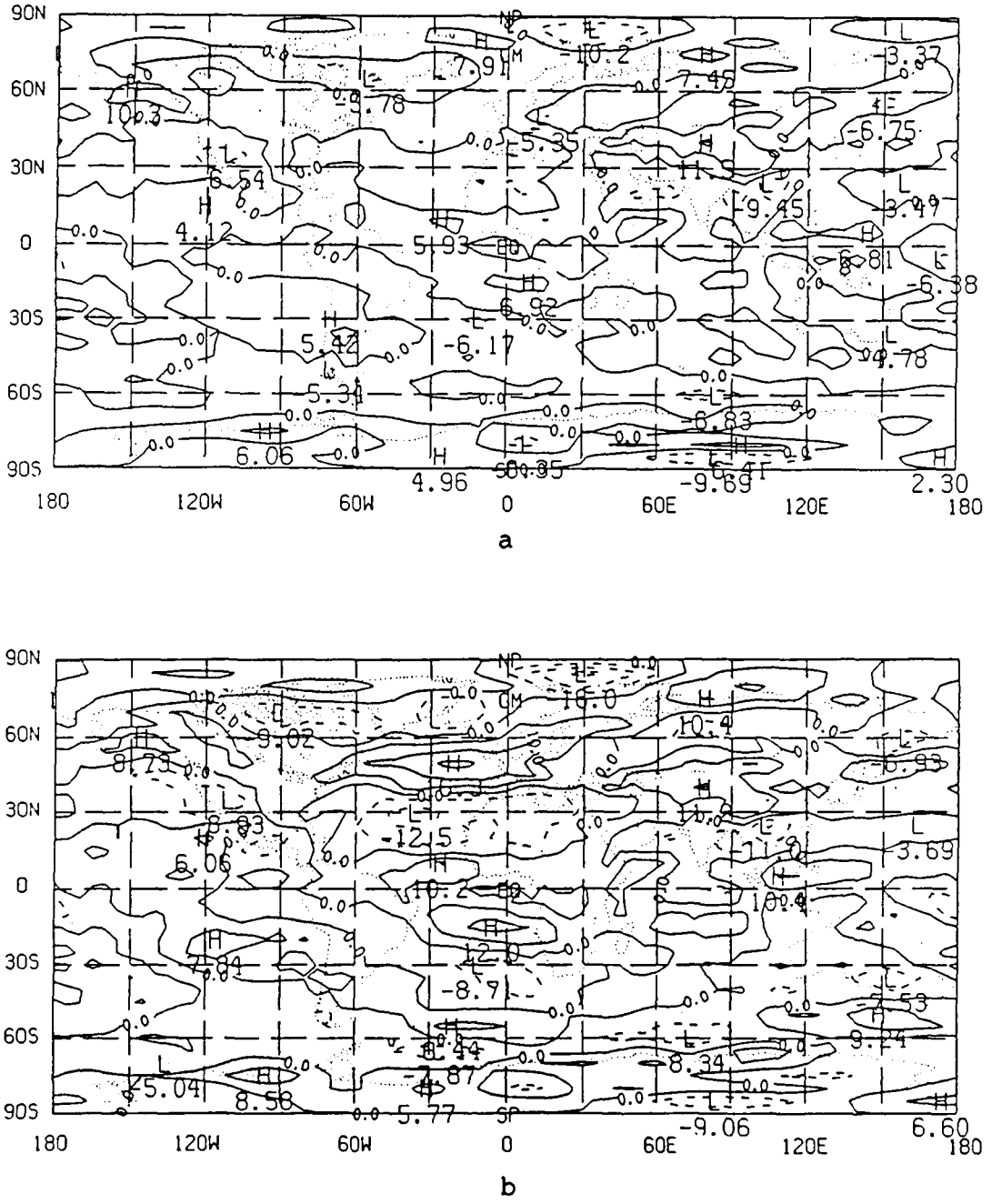

Figure 4.6. Average Case A error (m/s) in the 700 mb zonal wind (forecast minus analysis) for (a) pentad 1, (b) pentad 2, and (c) pentad 3. Contour interval = 5 m/s.

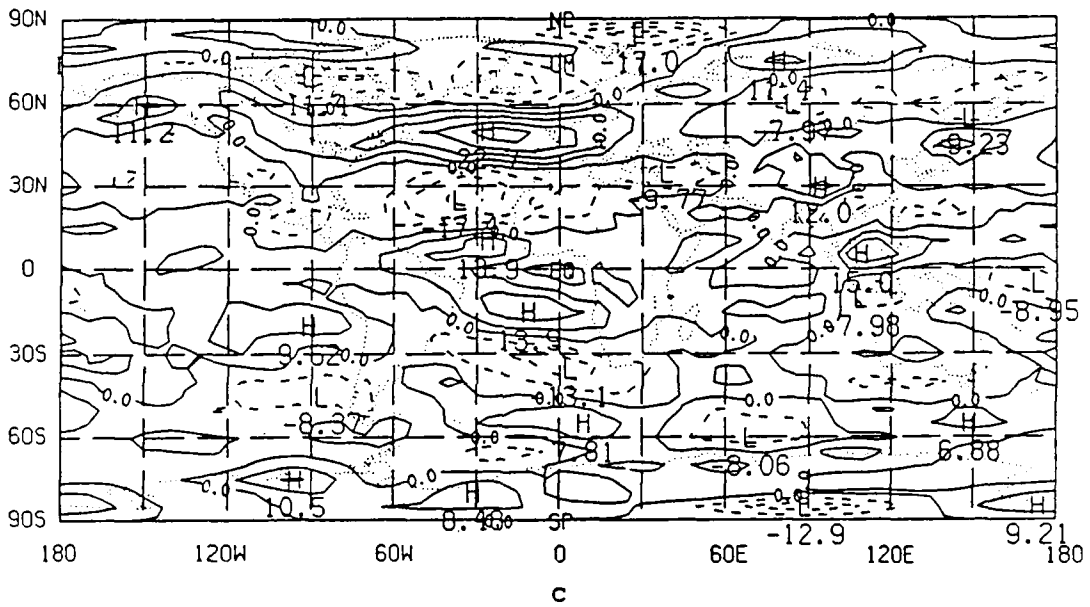

Figure 4.6. (continued).

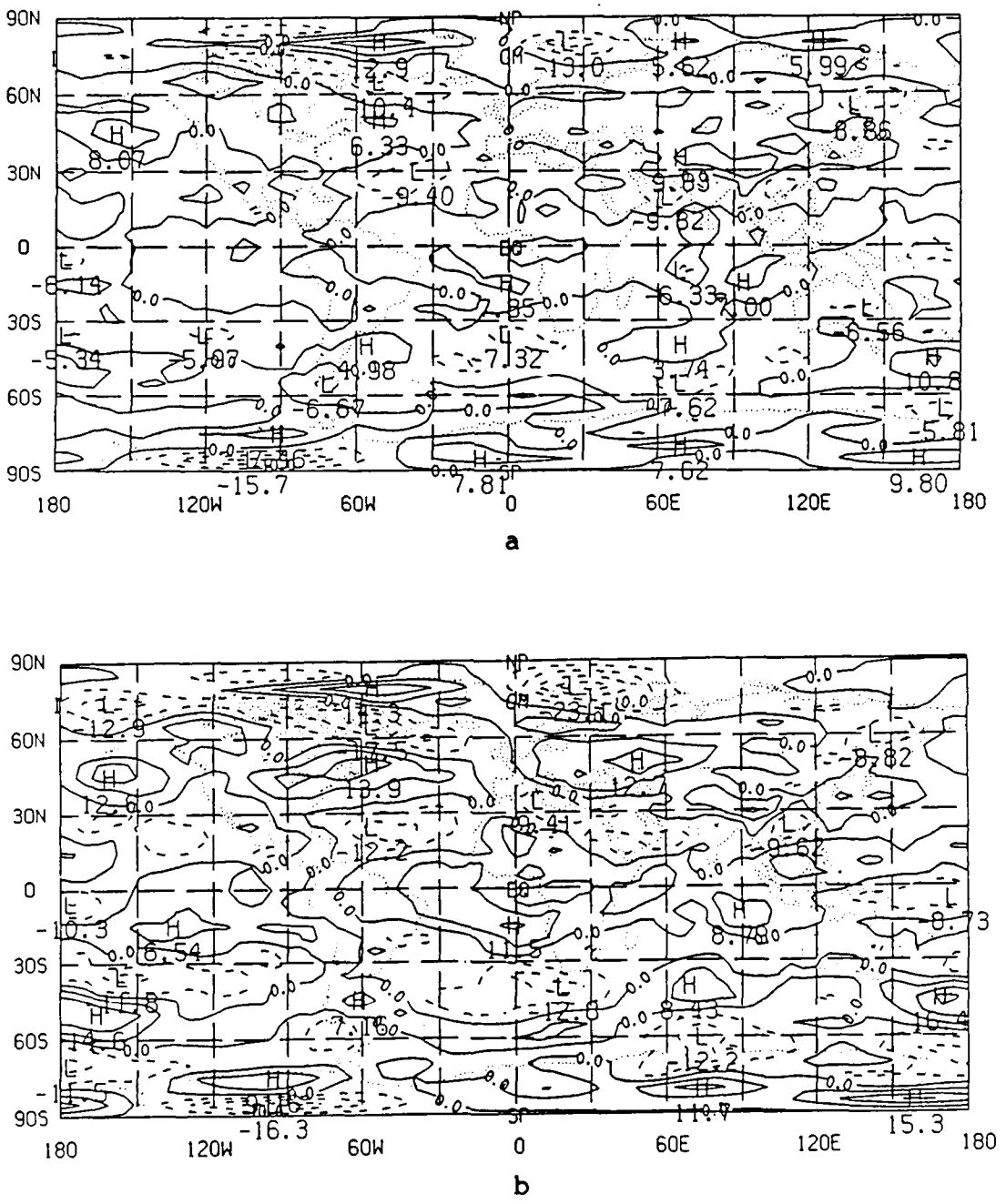

Figure 4.7. Average Case B error (m/s) in the 700 mb zonal wind (forecast minus analysis) for (a) pentad 1, (b) pentad 2, and (c) pentad 3. Contour interval = 5 m/s.

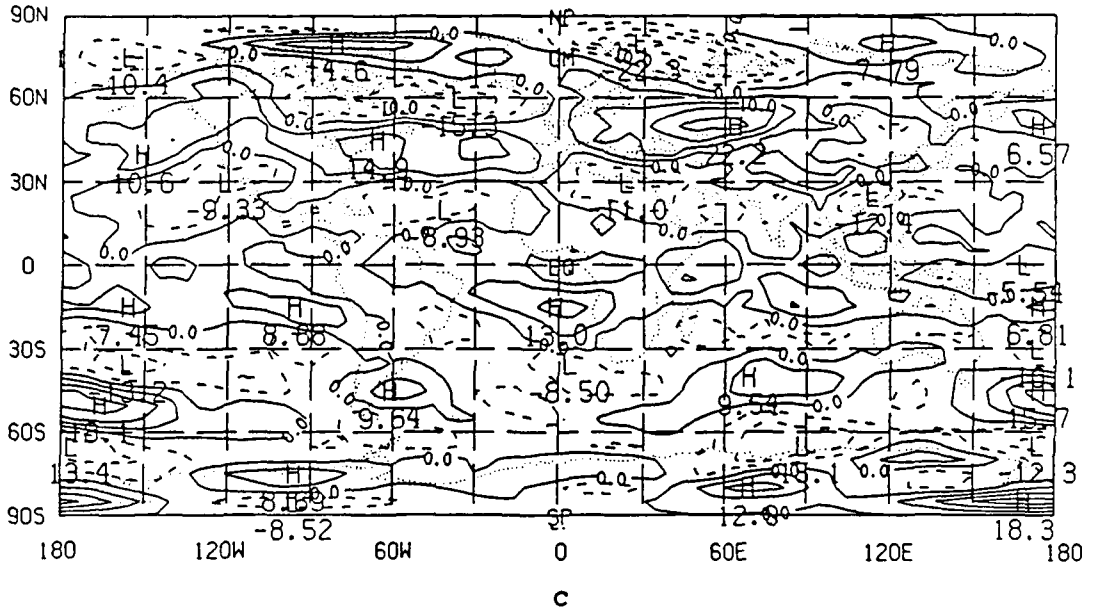

Figure 4.7. (continued).

circulations. To find out if there is error propagation between the extratropics and tropics, the pentad 2 zonal wind error is subtracted from the pentad 3 zonal wind error, and the pentad 1 error is subtracted from the pentad 2 error for the different modes, at $\sigma = .7$ and averaged for all individual cases of Case A and Case B, respectively. These error differences will show propagation patterns in the error field. The results for the external Rossby mode in Case A are shown in Fig. 4.8. There appears to be little interaction between the extratropics and the tropics. A very large positive error difference develops over the North Atlantic and remains basically stationary while it intensifies. This is associated with the large blocking ridge discussed earlier. A large positive error difference appears to move southeastward from the Bay of Bengal. While the large values are within the confines of the Northern Hemisphere, the error structure is such that it influences the northern tropics and gives the RMS difference previously discussed. A clear sign of extratropical/tropical interaction occurs over the southern Atlantic, off the coast of South America. An area of maximum error difference appears to propagate from the central Pacific (45° S, 145° W) northeastward to just off the coast of Peru (90° W, 15° S).

Error difference propagation in the external Rossby modes during Case B is shown in Fig. 4.9. Of special note is the large, positive error difference located over the central South Pacific near the date line (180°, 50° S), best seen in Fig. 4.9a. This is associated with the stationary high amplitude waves that developed during this time frame. More pronounced extratropical/tropical interactions are seen for this case. A stationary trough discussed earlier produces a large positve error difference along the northeast coast of the United States (70° W, 50° N). This error difference dives southeastward to the central Atlantic (45° W, 30° N). While the high center itself is still located in the Northern Hemisphere, the error

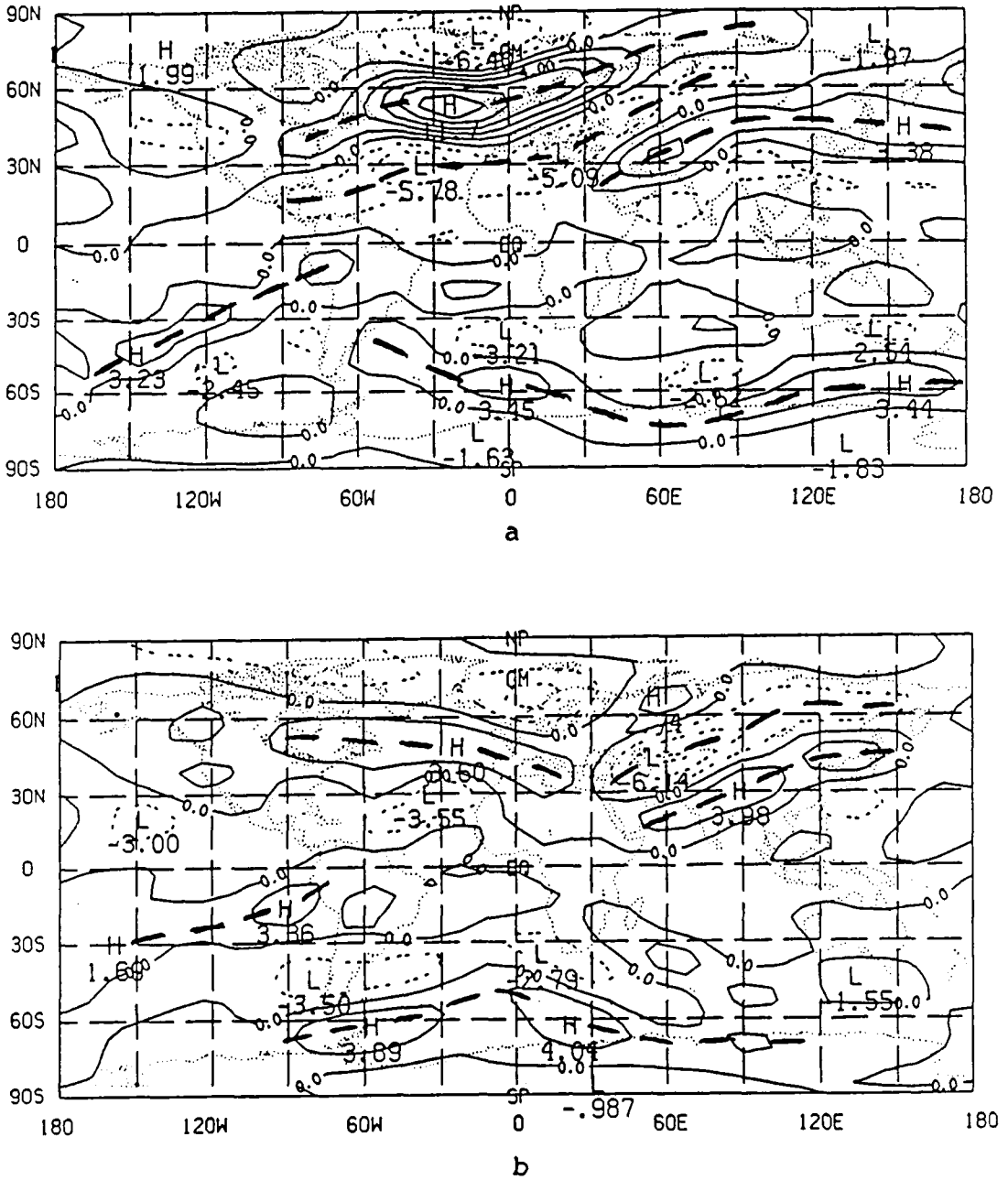

Figure 4.8. Case A $\sigma = .7$ average zonal wind error difference (m/s) in the external Rossby modes for (a) pentad 2 minus pentad 1 and (b) pentad 3 minus pentad 2. Contour interval = 2 m/s.

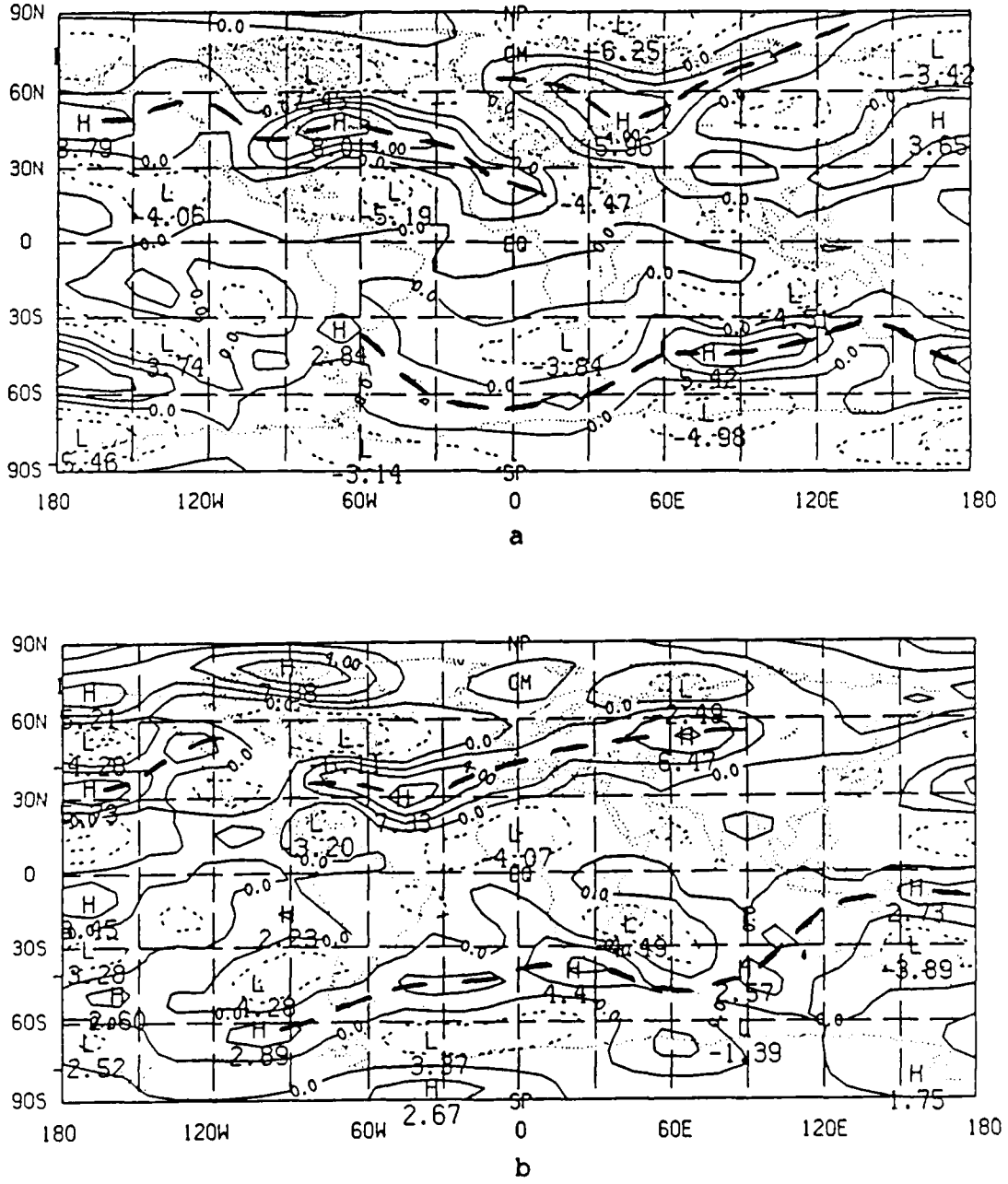

Figure 4.9. Case B $\sigma = .7$ average zonal wind error difference (m/s) in the external Rossby modes for (a) pentad 2 minus pentad 1 and (b) pentad 3 minus pentad 2. Contour interval = 2 m/s.

pattern associated with it does affect tropical latitudes. There also appears to be an equatorward movement of error centers in the central Pacific of the Northern Hemisphere. Most of the other error differences in the Northern Hemisphere are confined to this region. For example, a maximum error difference found in southern Asia (also associated with a blocking trough) propagates northeast into the Soviet Union. In the Southern Hemisphere, the propagation pattern appears to be more zonal in nature. However, there are exceptions to this. A negative error difference near the coast of South Africa (40° E, 40° S) moves northeastward to a positon over Madagascar (45° E, 20° S). Additionally, another negative error difference propagates from extreme western Australia (110° E, 20° S) to off the southeast coast of the continent (140° E, 30° S). Generally, there is more interaction between the tropics and extratropics than was noticeable in Case A.

Interactions between the tropics and the extratropics are more clearly seen in the internal Rossby modes. During Case A (Fig. 4.10), positive error differences along the west coast of the United States and Central America intensify and slide southeast to positions over the equator, merging with the error band that extends from South America to eastern Europe. These error patterns are noticeably smaller than those seen for the external Rossby modes, but represent about 54 percent of the internal Rossby mode contribution to the transient kinetic energy. The Case B error difference pattern (not shown) also shows more error propagation than the external modes.

The zonal wind error difference field for the EG modes during Case B is shown in Fig. 4.11, since this is the case with the largest tropical errors. It should be noted that the error values are about one-third of those seen in the internal Rossby modes. It appears as though a large negative error difference in the central Pacific (150° W, 10° N) splits in two, with one part moving north (150° W, 35° N), and

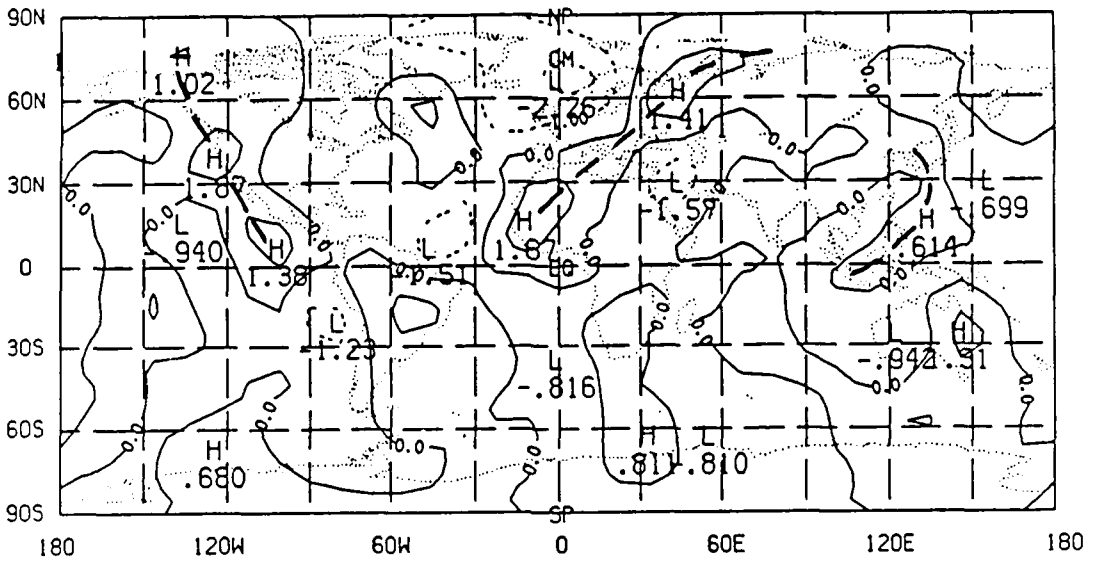

a

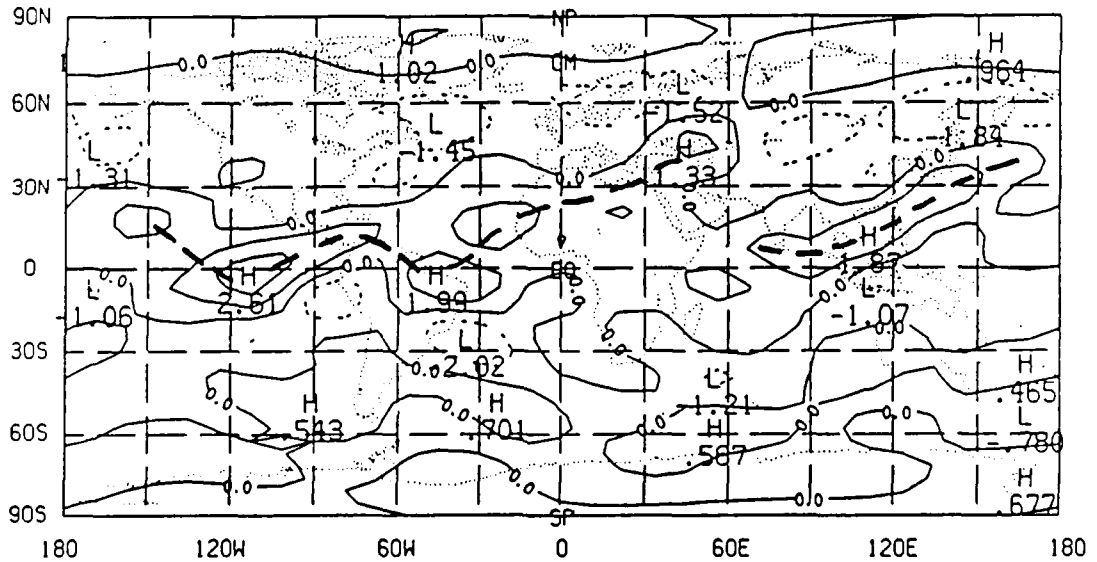

b

Figure 4.10. Case A $\sigma = .7$ average zonal wind error difference (m/s) in the internal Rossby modes for (a) pentad 2 minus pentad 1 and (b) pentad 3 minus pentad 2. Contour interval = 1 m/s.

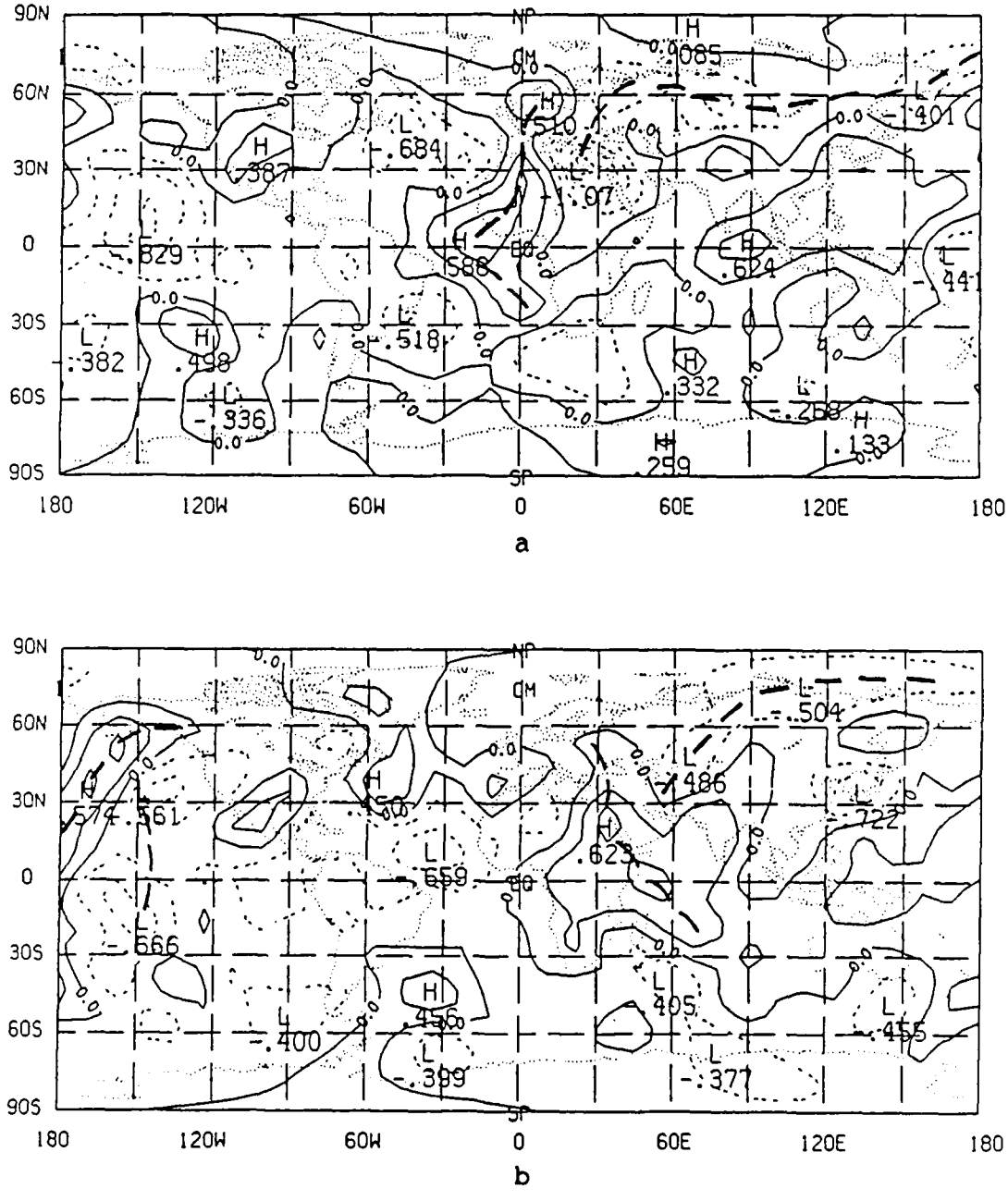

Figure 4.11. Case B $\sigma = .7$ average zonal wind error difference (m/s) in the internal eastward gravity modes for (a) pentad 2 minus pentad 1 and (b) pentad 3 minus pentad 2. Contour interval = .25 m/s.

the other south (150° W, 35° N). A positive error difference in the central part of the United States moves due east into the western Atlantic. A large negative error difference over Libya (20° E, 30° N) propagates northeastward into the southern part of the Soviet Union (70° E, 45° N). A large maximum error region extending from the equatorial Atlantic through western Africa and up into Europe, moves generally eastward into eastern Africa and the western Indian Ocean. However, the maximum difference center associated with this propagates in a distinct northeastward direction from (25° W, 5° N) to (35° E, 20° N). Thus, while interactions between the tropics and extratropics are noticeable in the EG modes, a large part of the tropical error reflects the model's lack of skill in simulating the intraseasonal oscillation.

Error difference fields for the meridional wind at $\sigma = .7$ will be examined next. The external Rossby modes for both case A and case B (Figs. 4.12 and 4.13, respectively) indicate that little tropical/extratropical interaction takes place. During Case A, a large error difference over Norway propagates southeastward to a position over the eastern Soviet Union. This error is associated with the large blocking ridge discussed earlier. A low center over southern Greenland (40° W, 70° N) also moves southeastward to a position off the coast of England (15° W, 45° N). Also of note is another low center that propagates northeastward from southern Asia (30° E, 40° N) to the central part of the Soviet Union (75° E, 50° N). While all these propagation patterns do display some meridional movement, they are all still confined to the Northern Hemisphere. The only hint of interaction between the Northern Hemisphere and the tropics occurs with the southward propagation of a high center from just off the northeast coast of Alaska (165° W, 75° N) to the central Pacific (165° W, 35° N). In the Southern Hemisphere, the propagation pattern is mainly zonal. During Case B (Fig. 4.13), the error difference patterns appear to generally

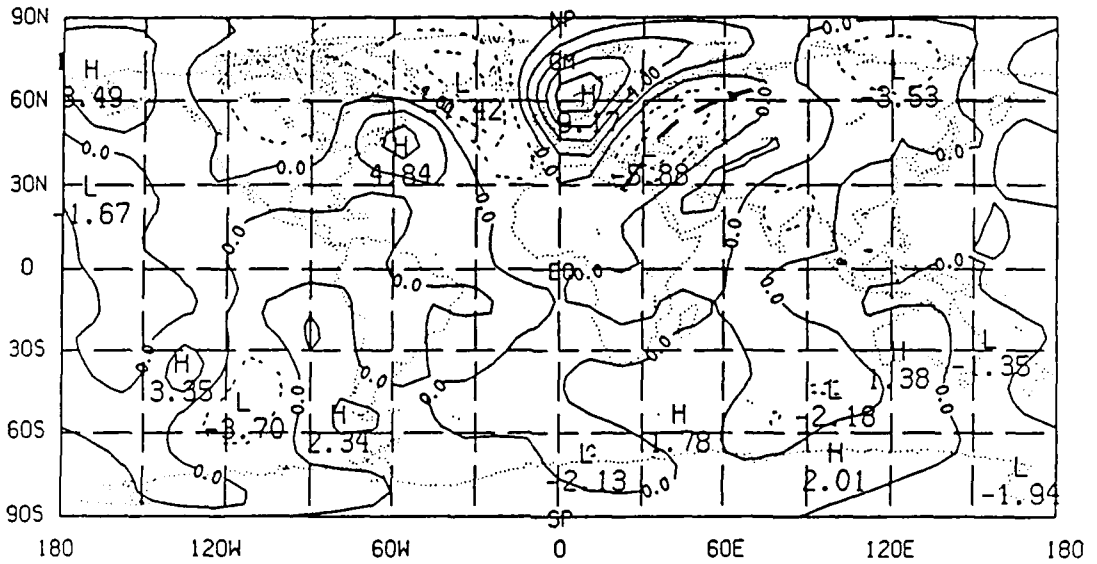

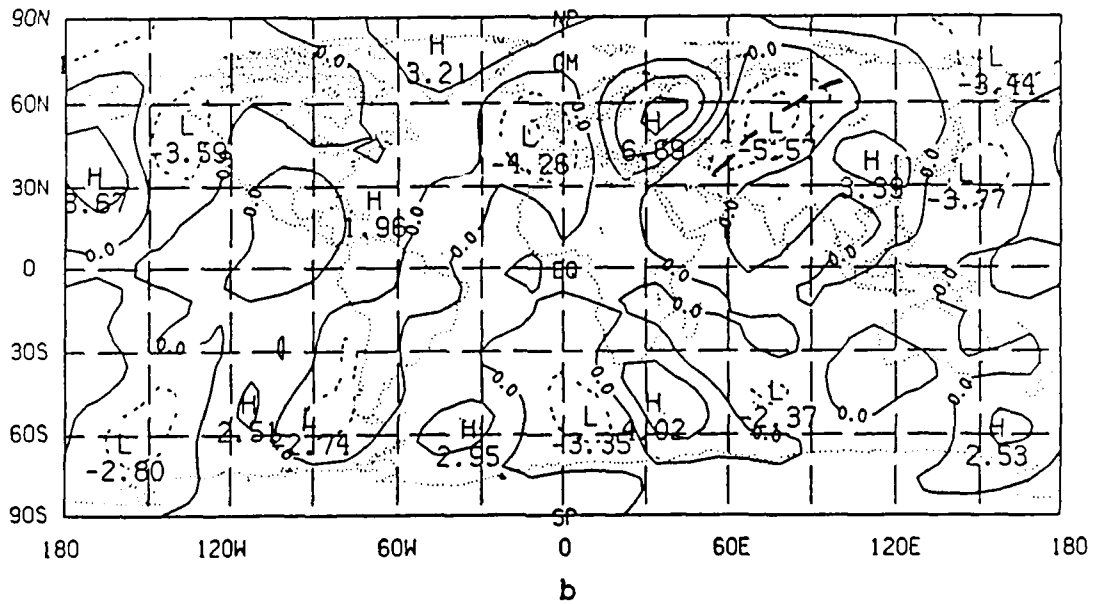

Figure 4.12. Case A σ = .7 average meridional wind error difference (m/s) in the external Rossby mode for (a) pentad 2 minus pentad 1 and (b) pentad 3 minus pentad 2. Contour interval = 2 m/s.

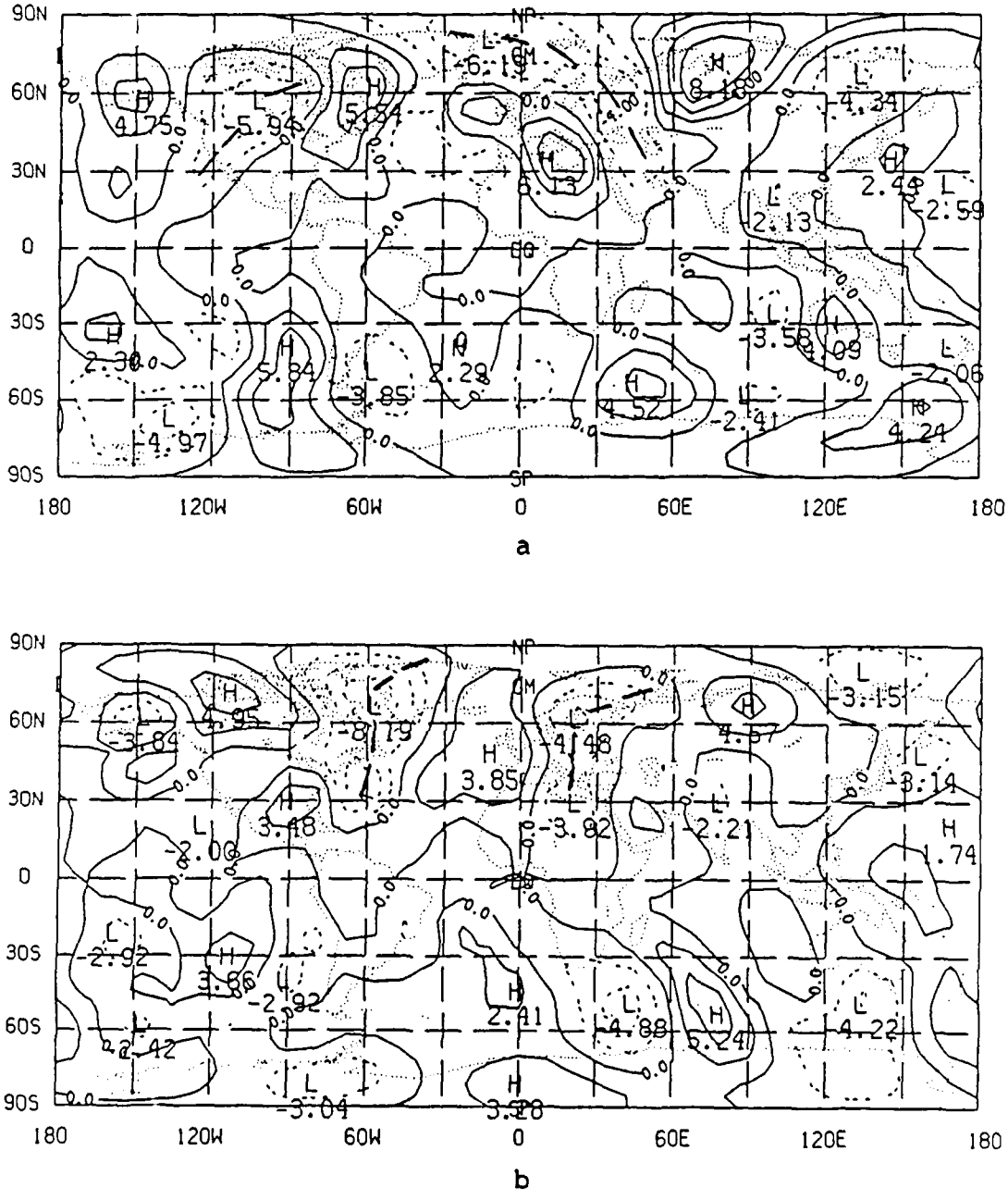

Figure 4.13. Case B σ = .7 average meridional wind error difference (m/s) in the external Rossby mode for (a) pentad 2 minus pentad 1 and (b) pentad 3 minus pentad 2. Contour interval = 2 m/s.

be confined to their respective hemispheres. No real interaction is noted.

In the internal Rossby modes, a strong link between the tropics and extratropics is seen. Figures 4.14 and 4.15 show the error difference in the meridional wind field for Case A and Case B, respectively. Error patterns obviously propagate both zonally and meridionally, with connections between the Northern Hemisphere, the tropics, and the Southern Hemisphere in both cases. These error patterns are certainly more global in nature than those in the external Rossby modes.

To summarize this section, error difference patterns in both the zonal and meridional wind at $\sigma = .7$ clearly show that the strongest interactions between the tropics and extratropics occur in the internal Rossby modes. The error patterns in the external Rossby modes are mostly stationary for the zonal wind and are generally confined to the hemisphere of origin, with significantly less global interaction.

4.6 Total Rainfall Errors

The model has a very strong tendency to over forecast precipitation amounts. Figures 4.16 and 4.17 show the differences in the total rainfall errors for Case A and Case B, respectively. As expected, most of the sizable errors are located in the tropics. Earlier DERF studies have found that the model has a strong cold bias over nearly the entire globe. The systematic error of over forecasting precipitation amounts suggests that global warming would be prevalent in the model. Additionally, the error difference patterns in the internal EG modes (Fig. 4.11) and the total rainfall do not correlate well, especially over the tropical Atlantic and across Africa. This suggests that the forcing and the dynamics may not be linked in these areas.

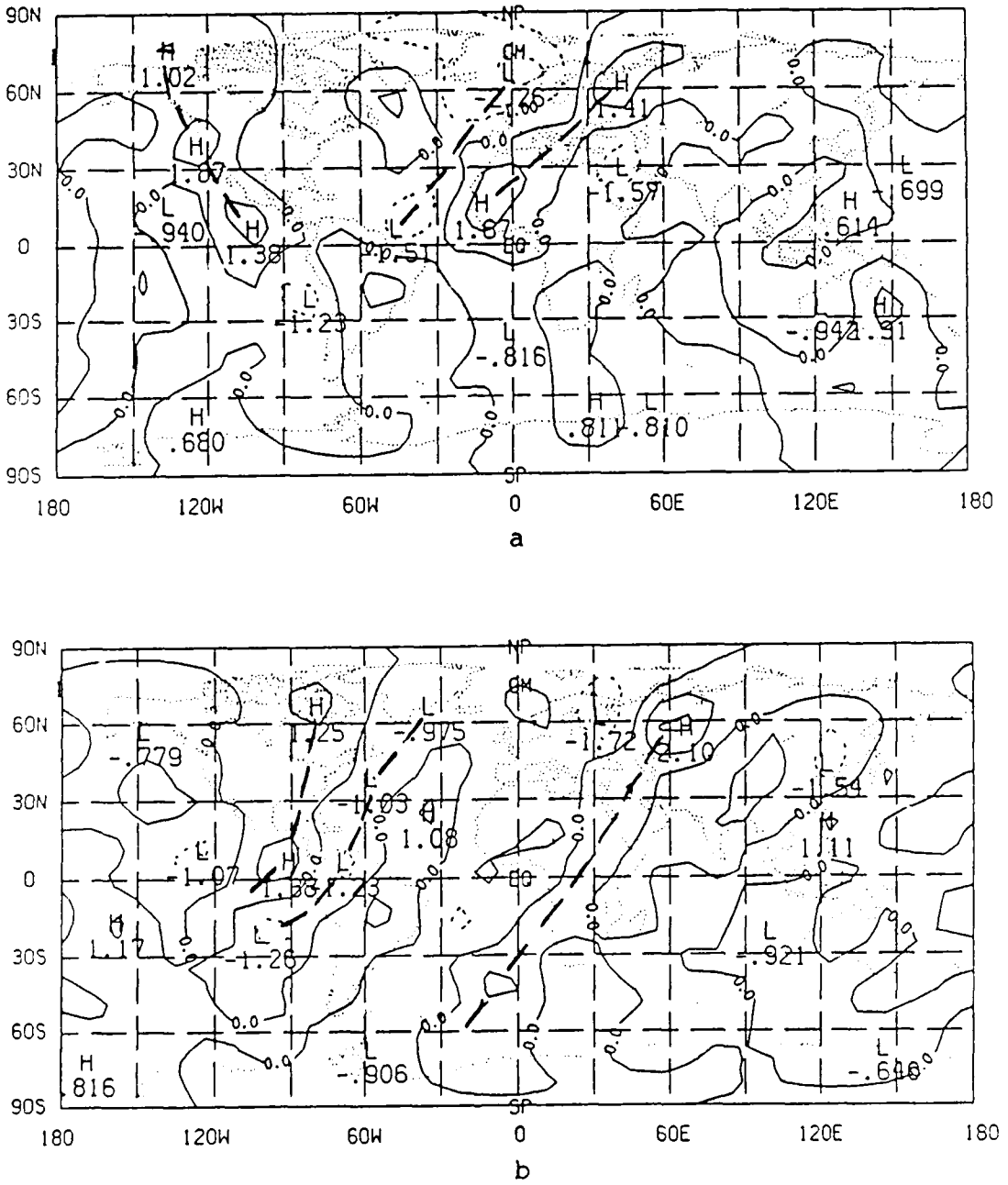

Figure 4.14. Case A $\sigma = .7$ average meridional wind error difference (m/s) in the internal Rossby modes for (a) pentad 2 minus pentad 1 and (b) pentad 3 minus pentad 2. Contour interval = 1 m/s.

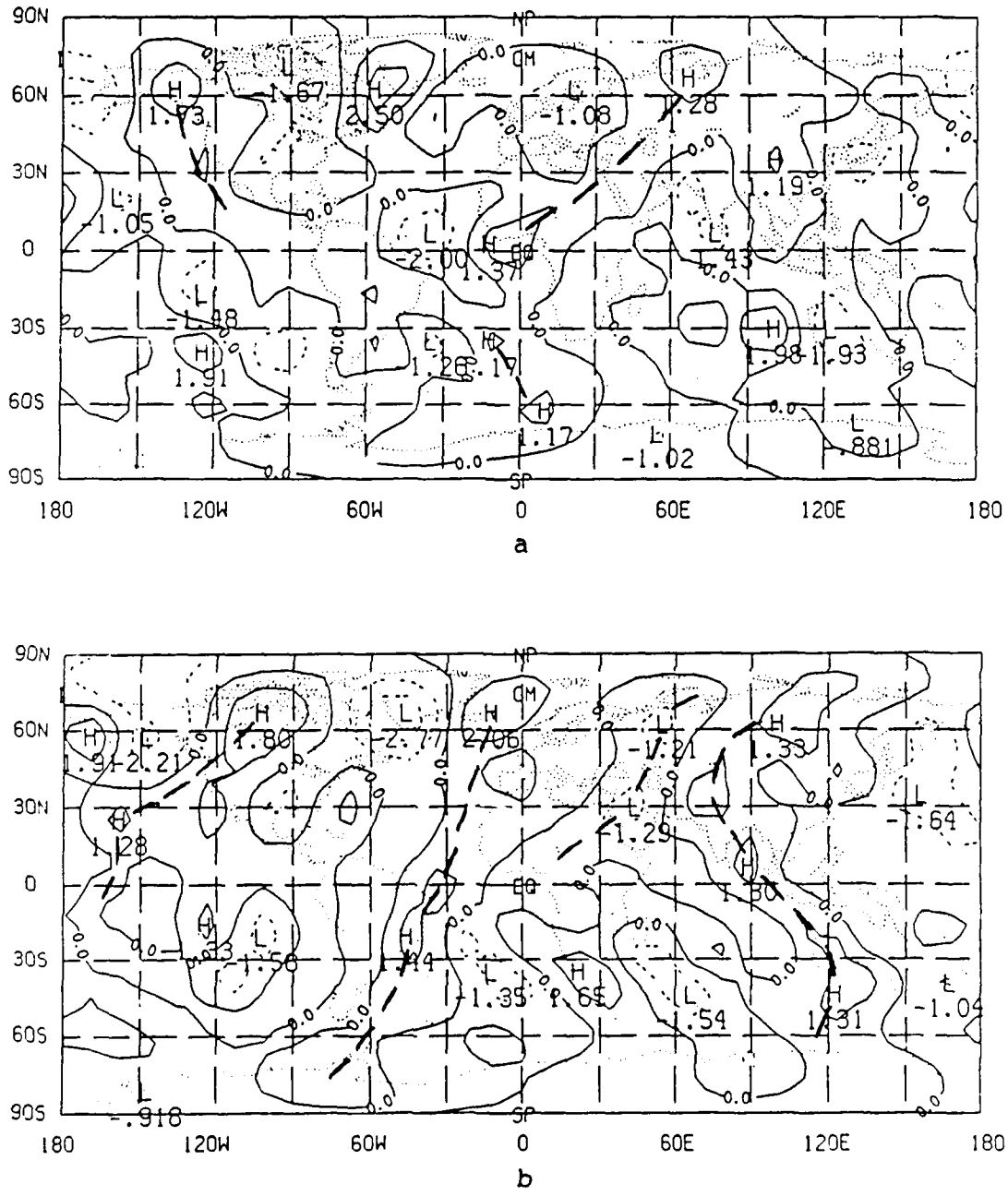

Figure 4.15. Case B σ = .7 average meridional wind error difference (m/s) in the internal Rossby modes for (a) pentad 2 minus pentad 1 and (b) pentad 3 minus pentad 2. Contour interval = 1 m/s.

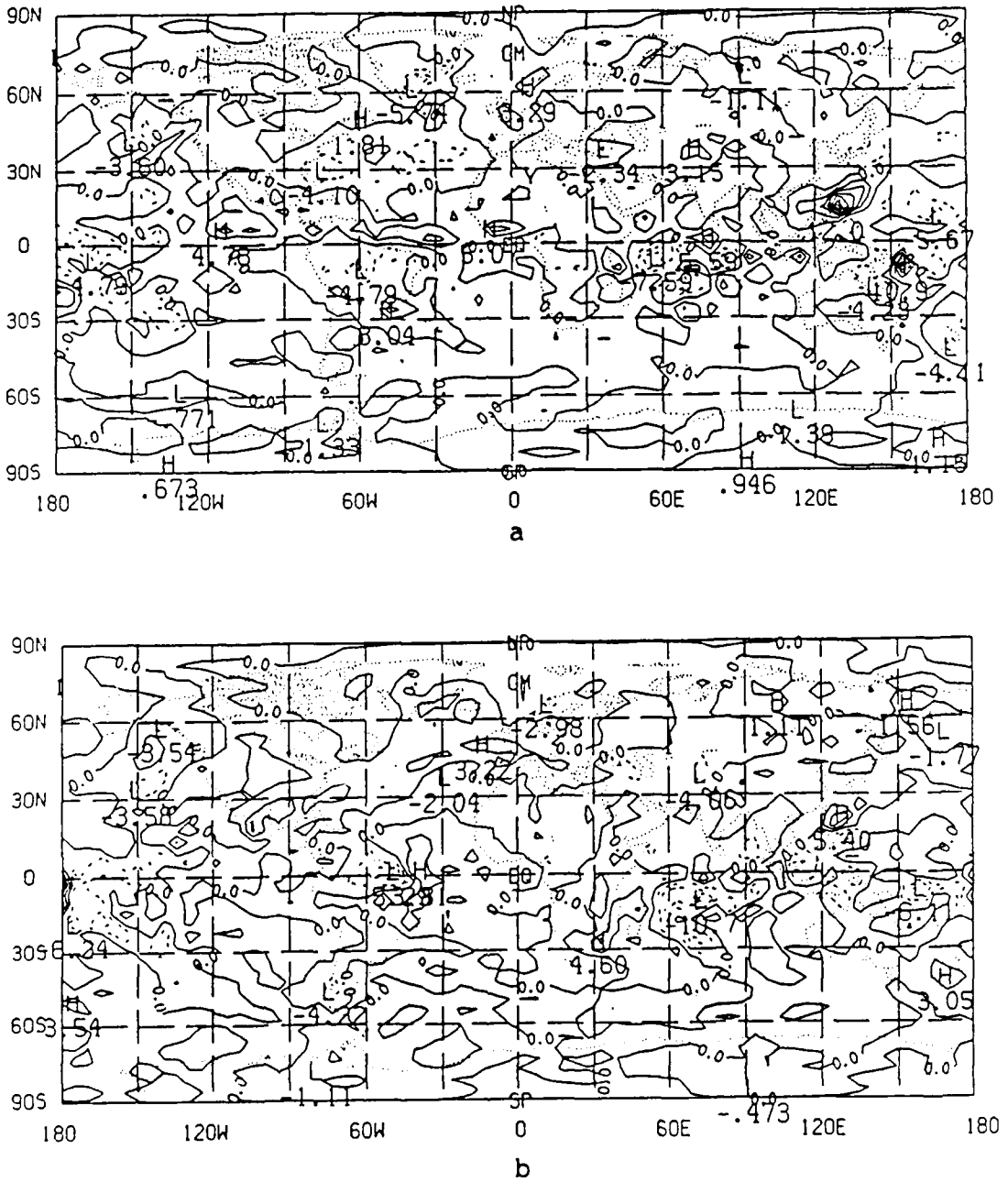

Figure 4.16. Case A average total rainfall error difference (mm/day) for (a) pentad 2 minus pentad 1 and (b) pentad 3 minus pentad 2. Contour interval = 2 mm/day.

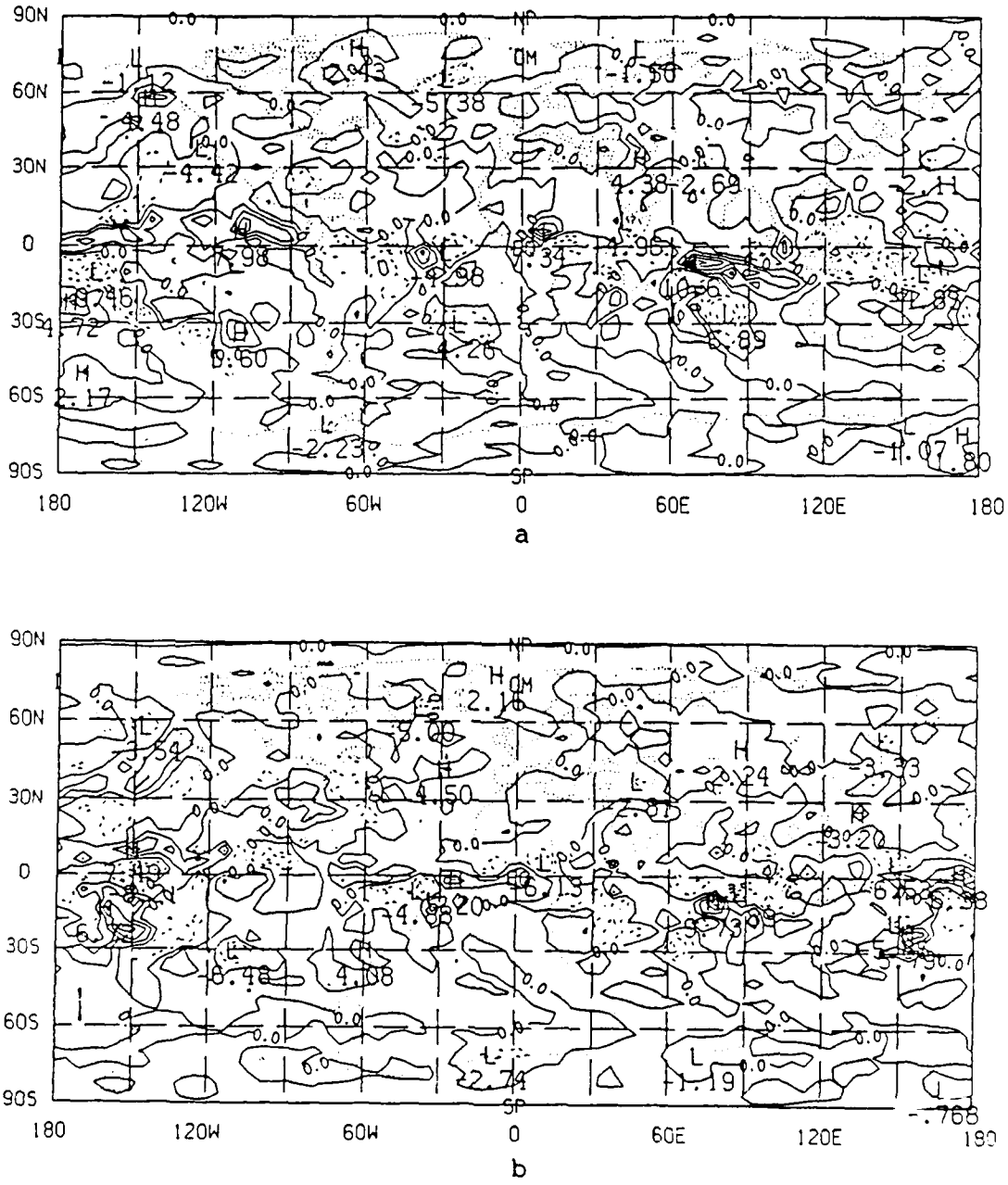

Figure 4.17. Case B average total rainfall error difference (mm/day) for (a) pentad 2 minus pentad 1 and (b) pentad 3 minus pentad 2. Contour interval = 2 mm/day.

CHAPTER 5

SUMMARY AND CONCLUSIONS

In this investigation, a reduced version of the DERF II data was analyzed to determine the accuracy of NMC model global forecasts, with emphasis on the 30-50 day oscillation. The diagnostic tool used was the projection of wind and height data onto the normal modes of a primitive equation model linerized about a basic state at rest and prescribed global temperature. This projection method was utilized because it offers many advantages over single variable analyses. First, the contributions from separate vertical modes can be considered on an individual basis. Also, the horizontal structures permit the simultaneous analysis of the wind and the mass fields, allowing the flow to be decomposed into two distinct types of motion: high frequency waves (inertia-gravity modes) and low frequency waves (rotational modes of the Rossby/Haurwitz type).

The strongest signature of the 30-50 day oscillation in the analysis data was found in pentad averages of the zonal wind anomalies at the tropics due to the internal gravity modes (which include the tropically trapped Kelvin mode). An important aspect of this study was to compare tropical and extratropical forecasts when the 30-50 day oscillation is strong and when it is quite weak. Comparison cases were selected from the the zonal wind anomaly data to isolate cases with small and large amplitude of the intraseasonal oscillation. The example of when the oscillation is weak and slow moving is called Case A. It begins on pentad 2 (17 Dec 86), requiring eight pentads to circle the globe. The case of a strong, rapidly

propagating oscillation is Case B. It required only five pentads to complete a global propagation, beginning on pentad 15 (20 Feb 87).

There were many important differences between these cases. During Case A, the Northern Hemisphere has large amplitude blocking patterns located over the eastern Atlantic Ocean and the western United States. In the Southern Hemisphere, the flow is more zonal in nature during this time. Case B shows a weakening of the blocking patterns in the Northern Hemisphere and the development of large amplitude waves in the Southern Hemisphere, over the central Pacific. These changes in the Northern Hemisphere flow are reflected in a study by Tracton et al. (1989), which showed the skill of persistence to be significantly greater for Case A than for Case B. It is also interesting to note that when the Northern Hemisphere experienced a more stationary wave pattern (Case A), the tropics were relatively calm, with a very weak signature of the 30-50 day oscillation.

During Case B, the Southern Hemisphere is just beginning to undergo the transition from summer to fall. Large amplitude stationary waves are present over the central Pacific Ocean. As a result, the tropical Pacific experienced much greater rainfall than was seen during Case A. This is demonstrated in the first 24 hour forecast of total rainfall, which reflects the overall global characteristics of precipitation.

Ferranti et al. (1990) showed that during certain phases of the 30-50 day oscillation, the interaction between the tropics and extratropics was most pronounced. They found that when the tropical forecasts are relaxed toward the analysis, improvement of skill is consistent with the percentage of mid-latitude variance explained by tropical/extratropical interactions. Additionally, when extratropical forecasts are relaxed towards the analysis, the forecast of the rotational flow in the tropics is generally improved.

Tsuyuki (1989) examined the relationship between the tropical 30-50 day oscillation and the quality of extratropical forecasts using the global prediction model of the Japan Meteorological Agency (JMA). He found that the model has great skill in forecasting the oscillation when it is significant in the observation. This is due to revisions in the model, which greatly improved the forecast of tropical divergent fields. When the 30-50 day oscillation is well-predicted, he found that extended range forecasts for the Northern Hemisphere show a marked improvement.

Does the NMC forecast model have skill in predicting these tropical/extratropical interactions? The normal mode projection used in this study allows this question to be addressed. This study has shown that the model does not do well in forecasting either the magnitude or propagation of the 30-50 day oscillation. Errors are apparent in the tropical divergent wind field (Kelvin mode), but no clear evidence was found showing that these error fields significantly influence the extratropics. Generally, the pattern has been for errors in the extratropics, especially in the Northern Hemisphere, to propagate into tropical regions. This is best seen in the internal Rossby modes. This agrees with the study by Ferranti et al. (1990), which showed that skillful forecasts in the extratropics has an effect on the rotational component of the tropical wind.

Table 5.1 shows the horizontal mode contribution to the total wind field at $\sigma = .7$. The external Rossby modes dominate the total wind in the extratropical regions. In the Northern Hemisphere, for example, the external Rossby modes make up around 56 percent of the total wind field and 65 percent of the total rotational flow. In the tropics, the internal Rossby modes contribute most to the total wind field. They contain over twice as much kinetic energy as that found in the internal EG modes. On the other hand, the internal EG modes contribute twice as much to the total tropical flow as does the internal WG component of the wind.

Table 5.1. DERF period zonally averaged root mean square total wind (m/s) at sigma = .7.

	Rossby Modes		Internal Gravity Modes	
	External	Internal	Eastward	Westward
Northern Hemisphere (20°N-80°N)	40.0	21.6	5.5	4.4
Tropics (20°N-20°S)	13.1	14.2	6.8	3.1
Southern Hemisphere (20°S-80°S)	33.3	11.1	3.3	3.0

The horizontal mode contribution to the transient component of the wind (mean zonal flow removed) at $\sigma = .7$ is shown in Table 5.2. The external Rossby modes dominate the transient wind in the tropics as well as the extratropics.

The error in the $\sigma = .7$ wind of the Northern Hemisphere is nearly three times higher for the external Rossby modes than for the internal Rossby modes. However, the internal Rossby modes constitute only about 35 percent of the total rotational flow in the extratropics of the Northern Hemisphere. It was shown that errors in the internal Rossby modes were very transient in nature, while the external Rossby error was generally stationary. Based upon this, the internal Rossby contribution to the error field is actually quite large compared to the external Rossby contribution. The internal Rossby error patterns represent around 54 percent of the internal Rossby mode contribution to the transient kinetic energy. On the other hand, the external Rossby errors only represent about 44 percent of the external Rossby contribution to the kinetic energy of the mean flow (see Table 5.3).

In the tropics, the error in the $\sigma = .7$ wind is again larger for the external Rossby modes than the internal Rossby modes. However, in this case the difference is not nearly as large (27 percent). The internal Rossby modes contain nearly 52 percent of the rotational flow in the tropics. The internal Rossby error values represent about 42 percent of the internal Rossby mode contribution to the total kinetic energy. The external Rossby errors represent about 61 percent of the external Rossby mode contribution to the total kinetic energy (see Table 5.3).

Improvements in extratropical forecasts will be obtained when rotational motions are better specified. Past studies have claimed that the key to improving extratropical forecasts is to reduce the error in the external Rossby modes. However, this study shows that while the internal Rossby modes contain only 35 percent of the wind, the error associated with these modes is significant when compared to

Table 5.2. DERF period zonally averaged root mean square transient wind (m/s) at sigma = .7.

	Rossby Modes		Internal Gravity Modes	
	External	Internal	Eastward	Westward
Northern Hemisphere (20°N-80°N)	18.2	6.6	2.4	2.5
Tropics (20°N-20°S)	8.6	6.3	2.4	1.2
Southern Hemisphere	14.7	6.0	1.5	1.7

Table 5.3. Contributions of rotational modes at sigma = .7 in the Northern Hemisphere extratropics and the tropics.

	Northern Hemisphere Extratropics (20°N-80°)		Tropics (20°N-20°S)	
	Internal Rossby	External Rossby	Internal Rossby	External Rossby
Percent of Total Flow	30%	56%	38%	36%
Percent of Total Rotational Flow	35%	65%	52%	48%
Error Representation of Mode Contribution to Total Kinetic Energy	16%	25%	42%	61%
Error Representation of Mode Contribution to Transient Kinetic Energy	54%		100%	
Error Representation of Mode Contribution to Mean Flow Kinetic Energy		44%		172%

the external Rossby components. Perhaps more emphasis should be placed on improving the simulation of the internal Rossby modes in these regions.

Rotational error fields in the tropics closely resemble their extratropical counterparts (especially the Northern Hemisphere). This indicates that most of the errors in these modes are imported from the extratropics. Improvement in the specification of tropical phenomenon is expected to result in better forecasts of the divergent wind components, which are not due to the influences of the extratropics. Interestingly enough, the error in the tropical Kelvin mode saturates at pentad 2, and then decreases in magnitude. Thus, it appears as though adjustments are being made in the model, with a return of forecasting skill as time goes on. This, however, may be due to the fact that the number of individual forcast cases considered is quite small.

REFERENCES

Chen, T. -C., and J. C. Alpert, 1989: The systematic errors of annual and intraseasonal variations of the planetary-scale divergent circulation in NMC medium range forecasts (in preparation).

Chen, W. Y., 1989: Estimate of dynamical predictability from NMC DERF experiments. *Mon. Wea. Rev.*, **117**, 1227-1236.

Emanuel, K. A., 1987: An air-sea interaction model of intraseasonal oscillations in the tropics. *J. Atmos. Sci.*, **44**, 2334-2340.

Ferranti, L., T. N. Palmer, F. Molteni and E. Klinker, 1990: Tropical-extratropical interaction associated with the 30-60 day oscillation, and its impact on medium and extended range predictability. Submitted to *J. Atmos. Sci.*

Hayashi, Y. -Y., and A. Sumi, 1986: The 30-40 day oscillations simulated in an aqua planet model. *J. Meteor. Soc. Jpn.*, **64**, 451-466.

Kalnay, E., R. Gardner, H. -L. Pan, M. Kanamitsu and G. White, 1988: Precipitation and surface properties in the NMC global model: systematic characteristics and predictability. *WGNE Workshop on Model Systematic Errors*, Toronto, Canada, September 19-23, 1988.

Kasahara, A., 1979: Normal modes of ultralong waves in the Atmosphere. *Mon. Wea. Rev.*, **104**, 669-690.

___, and K. Puri, 1981: Spectral representation of three-dimentional global data by expansion in normal mode funcitons. *Mon. Wea. Rev.*, **109**, 37-51.

Lau, K. -M., and P. H. Chan, 1985: Aspects of the 40-50 day oscillation during the northern winter as inferred from outgoing longwave radiation. *Mon. Wea. Rev.*, **113**, 1889-1909.

Lee, B. -C., 1987: Observed normal mode structure of low frequency oscillations. Doctoral dissertation, University of Utah, 160 pp.

Lorenz, E. N., 1968: The predictability of a flow which possesses many scales of motion. *Tellus*, **21**, 289-307.

Madden, R. A., and P. A. Julian, 1971: Detection of a 40-50 day oscillation in the zonal wind in the tropical pacific. *J. Atmos. Sci.*, **28**, 702-708.

___, and___, 1972: Description of global-scale circulation cells in the tropics with a 40-50 day period. *J. Atmos. Sci.*, **29**, 1109-1121.

Matsuno, T., 1966: Quasi-geostrophic motions in the equatrial area. *J. Meteor. Soc. Jpn.*, **44**, 25-42.

Neelin, J. D., I. M. Held and K. H. Cook, 1987: Evaporation-wind feedback and low-frequency variability in the tropical atmosphere. *J. Atmos. Sci.*, **16**, 2341-2348.

Nogues-Paegle, J., B. -C. Lee and V. E. Kousky, 1989: Observed modal characterisitcs of the intraseasonal oscillation. *J. of Clim.*, **2** 496-507.

Roads, J. O., 1986: Forecasts of time averages with a numerical prediction model. *J. Atmos. Sci.*, **43**, 871-892.

Schubert, S., F. -C. Chang, W. Lau and R. Kistler, 1988: A reduced version of the DERF II data. *NASA Technical Memo*, June 1988, 27 pp.

Tracton, M. S., K. Mo, W. Chen, E. Kalnay, R. Kistler and G. White, 1989: Dynamical extended range forecasting (DERF) at the National Meteorological Center. *Mon. Wea. Rev.*, **117**, 1604-1635.

Tsuyuki, T., 1989: Prediction of the 30-60 day oscillation with the JMA global model and its impact on extended range forecast. Submitted to *J. Meteor. Soc. Jpn.*

END